

1 **Thalamus drives two complementary input strata of the neocortex in parallel**

2

3 R. Egger<sup>1†‡</sup>, R.T. Narayanan<sup>1†</sup>, D. Udvary<sup>1</sup>, A. Bast<sup>1</sup>, J.M. Guest<sup>1</sup>, S. Das<sup>2</sup>, C.P.J. de Kock<sup>2</sup>, M.  
4 Oberlaender<sup>1\*</sup>

5

6 <sup>1</sup>Max Planck Group: In Silico Brain Sciences, Center of Advanced European Studies and Research,  
7 Bonn, Germany; <sup>2</sup>Department of Integrative Neurophysiology, Center for Neurogenomics and Cognitive  
8 Research, VU Amsterdam, The Netherlands.

9

10 **Short title: The deep input stratum of the neocortex**

11 **Key words:** barrel cortex, pyramidal tract neurons, corticocortical neurons, whisker touch, in silico

12

13 † **these authors contributed equally** (in alphabetical order)

14 ‡ current address: Neuroscience Institute, NYU School of Medicine, New York, USA.

15

16 \* **Editorial correspondence:**

17 Max Planck Group: In Silico Brain Sciences

18 Center of Advanced European Studies and Research (caesar)

19 Ludwig-Erhard-Allee 2, Bonn, 53175 Germany

20 [marcel.oberlaender@caesar.de](mailto:marcel.oberlaender@caesar.de)

21

22 **Sensory information enters the neocortex via thalamocortical axons that define the major ‘input’**  
23 **layer 4. The same thalamocortical axons, however, additionally innervate the deep ‘output’ layers**  
24 **5/6. How such bistratification impacts cortical processing remains unknown. Here, we find a class**  
25 **of neurons that cluster specifically around thalamocortical axons at the layer 5/6 border. We show**  
26 **that these *border stratum cells* are characterized by extensive horizontal axons, that they receive**  
27 **strong convergent input from the thalamus, and that this input is sufficient to drive reliable**  
28 **sensory-evoked responses, which precede those in layer 4. These cells are hence strategically**  
29 **placed to amplify and relay thalamocortical inputs across the cortical area, for example to drive**  
30 **the fast onsets of cortical output patterns. Layer 4 is therefore not the sole starting point of**  
31 **cortical processing. Instead, parallel activation of layer 4 and the border stratum is necessary to**  
32 **broadcast information out of the neocortex.**

## 33 Introduction

34 The mammalian neocortex is required for higher-order brain functions, such as sensory perception and  
35 cognition, and hence for the transformation of information from the environment into behavior. Such  
36 information, for example as evoked by photo- or mechanoreceptor cells at the periphery of the visual or  
37 somatosensory system, enters the neocortex in form of a synchronous volley of excitation, which is  
38 provided by relay cells that are located in sensory system-specific primary nuclei of the thalamus <sup>1</sup>.  
39 Despite several species- and sensory system-specific differences, thalamocortical axons of relay cells  
40 terminate in general most densely in layer 4 of the respective primary sensory areas of the neocortex <sup>2</sup>.  
41 For decades, concepts about the neocortex thus focused on layer 4 as its main input site, and starting  
42 point of sensory information processing <sup>3</sup>. However, anatomical studies in macaques <sup>4</sup>, cats <sup>5</sup>, and rodents  
43 <sup>6</sup> indicate that the very same thalamocortical axons give rise to a second innervation peak at specific  
44 depth locations in the deeper layers 5 and/or 6. These layers represent the main output site of the  
45 neocortex, as they comprise long-range projection neurons that innervate subcortical brain structures <sup>2</sup>.

46  
47 The relevance of bistratified thalamocortical input for cortical information processing – and in particular  
48 of the deep input stratum within the output layers – remains poorly understood <sup>7</sup>. However, this knowledge  
49 is fundamental for deducing the logic of intracortical signal flow, for revealing the origin of cell type- and  
50 layer-specific neuronal activity patterns, and for constraining hypotheses of cortical circuit organization.  
51 So far, to our knowledge, no study has yet systematically investigated the principles by which a deep  
52 thalamocortical input stratum contributes to the overall sensory-evoked cortical excitation. It remains  
53 therefore unknown whether and how different types of neurons in the output layers can be driven directly  
54 by thalamocortical input, and if that would be the case, how responses in the deep input stratum affect  
55 those in the upper layers and vice versa.

56  
57 Here, we address these questions in the whisker somatosensory system of the rat <sup>8</sup>. Tactile information  
58 from whisker touch enters the neocortex via relay cells from the ventral posterior medial nucleus (VPM)  
59 of the thalamus <sup>2</sup>. Axons from these relay cells delineate layer 4 of the whisker-related part of the primary  
60 somatosensory cortex (wS1). Within layer 4, excitatory spiny neurons cluster around the dense terminal  
61 fields of the VPM axons. Upon sensory stimulation, this major thalamorecipient population gives rise to  
62 recurrent excitation within layer 4 and feed-forward excitation to the superficial layers 2/3 – a canonical  
63 organizational principle of all sensory cortices <sup>3</sup>. VPM axons show a second, less dense innervation peak  
64 in the deeper layers <sup>6</sup>. The VPM-to-wS1 pathway in rodents hence represents an ideal model system to  
65 elucidate the relevance of bistratified thalamocortical input for cortical sensory information processing.

66

67 Combining *in vivo* recordings with morphological reconstructions, optogenetic input mappings,  
68 pharmacological manipulations, and simulations of cortical signal flow, we reveal that – similar to the  
69 organization of layer 4 – thalamocortical inputs converge strongly onto a population of corticocortical cells  
70 that is strategically placed around the terminal fields of VPM axons at the layer 5/6 border. Upon sensory  
71 stimulation, this deep thalamorecipient pathway is activated first, evoking a stream of excitation that  
72 spreads horizontally across the deep layers, and which thereby precedes the vertical stream of signal  
73 flow through the canonical layer 4 to layers 2/3 pathway. Neuronal responses in primary sensory cortices  
74 may thus be regarded as a superposition of inputs from two simultaneously active primary thalamocortical  
75 pathways, which likely complement each other to ensure that intracortical computations are reliably  
76 transformed into cortical output patterns.

77

## 78 **Results**

### 79 **Corticocortical cells cluster around deep layer thalamocortical axons**

80 We compared the soma, dendrite, and axon distributions of all major excitatory cortical cell types <sup>2</sup> with  
81 the distributions of thalamocortical axons, and precise measurements of the cytoarchitectonic layer  
82 borders (**Fig. S1**) – anatomical data that we had systematically collected for one set of experimental  
83 conditions over the past decade in rat VPM and wS1 <sup>6, 9, 10, 11, 12, 13, 14</sup>. The comparison revealed that the  
84 peak density of VPM axons in the deep layers coincides with the cytoarchitectonic border between layers  
85 5 and 6 (**Fig. 1A**). Moreover, the soma depth distribution of layer 6 corticocortical (i.e., intratelencephalic)  
86 neurons matches the vertical extent of the deep layer VPM axon density peak (**Fig. 1B**). Neurons of this  
87 class are hence not restricted to layer 6, but equally abundant in lower layer 5 and upper layer 6.

88

89 These layer 5/6 corticocortical neurons can be easily distinguished from the subcortically projecting  
90 cortical output neurons that are found at the same depth: layer 5 pyramidal tract and layer 6  
91 corticothalamic neurons. First, by the characteristic morphology of their apical dendrites (**Fig. 1C**), which  
92 terminate in layer 4 without forming a tuft. This property also distinguishes them from polymorphic  
93 corticocortical neurons in deeper regions of layer 6 <sup>12</sup>. Second, by their extensive horizontally projecting  
94 axons (**Fig. 1D**), which can span across the deep layers of the entire cortical area (**Fig. 1E**). Our data  
95 reveal that analogously to the organization of excitatory populations in the major thalamorecipient layer,  
96 neurons with dendrite morphologies similar to those in layer 4, but with complementary intracortical axon  
97 projection patterns, cluster around thalamocortical axons in the deep layers. Together, VPM axons and  
98 layer 5/6 corticocortical neurons thus provide the structural basis of a deep thalamorecipient pathway for  
99 sensory-evoked signal flow, which we subsequently refer to as the '*layer 5/6 border stratum*' <sup>4</sup>.

100

## 101 **Thalamocortical inputs converge strongly onto border stratum cells**

102 Functional and anatomical studies in the rodent somatosensory<sup>7, 15</sup> and visual systems<sup>16</sup> suggest that  
103 neurons of all excitatory cell types that are located at the depth of the border stratum can receive direct  
104 input from the respective primary thalamic nuclei. We therefore quantified the degree to which border  
105 stratum cells (i.e., layer 5/6 corticocortical) in rat wS1 form monosynaptic connections with VPM axons,  
106 and investigated whether these synapses are functional under *in vivo* conditions. We expressed light-  
107 gated ion channels and a fluorescent marker within the thalamocortical synapses by injecting an adeno-  
108 associated virus into the VPM (**Fig. 2A**). Light-evoked and sensory-evoked action potential (AP)  
109 responses of individual wS1 neurons were obtained via cell-attached recordings in anesthetized rats (**Fig.**  
110 **2B**). Following the recordings, neurons were filled *in vivo* with biocytin, which allowed for post-hoc  
111 reconstruction and classification of the neurons' morphology (**Fig. 2C**), and detection of the putative  
112 thalamocortical synapses along the dendrites of the recorded neurons (**Fig. 2D**).

113  
114 The experiments revealed that  $7\pm 2\%$  of the spines along the dendrites of a border stratum cell receive  
115 input from the VPM (**Fig. 2E**). Similar fractions ( $10\pm 4\%$ ) and dendritic distributions of VPM synapses have  
116 been reported previously for spiny neurons in layer 4 of rat wS1<sup>17</sup>. Thus, the excitatory populations that  
117 define the respective postsynaptic parts of the two thalamocortical input strata – layer 4 spiny neurons  
118 and layer 5/6 border stratum cells – receive similar relative amounts of VPM input. Supporting these  
119 anatomical observations, light stimulation of VPM synapses elicited APs in the morphologically identified  
120 border stratum cells. The responses were equally reliable and as fast as those in layer 4 spiny neurons  
121 (**Fig. 2F**). The same border stratum cells also responded to sensory stimuli, as evoked by a low pressure  
122 airpuff that deflects all whiskers caudally. Under these conditions, sensory responses in border stratum  
123 cells were more reliable compared to those of spiny neurons in layer 4, and even rivaled the reliability of  
124 relay cells in the VPM (**Fig. 2G**). Our data reveal that analogously to layer 4 (**Fig. S2**), the strategic  
125 location of border stratum cells results in strong convergent input from primary thalamocortical axons,  
126 which provides the synaptic basis of a deep thalamorecipient pathway for sensory-evoked signal flow.

127

## 128 **Border stratum cells respond first to sensory stimuli**

129 Whole-cell recordings in rodent wS1<sup>18</sup> and V1<sup>16</sup> indicate that deep layer corticocortical neurons have  
130 intrinsic physiological properties that render them as highly excitable when compared to corticothalamic  
131 neurons that are found at the same depth. Together with our observation of strong convergence of  
132 thalamocortical axons, this suggests that synaptic input from these fibers may be sufficient to drive  
133 reliable sensory-evoked responses in border stratum cells (e.g. those shown in **Fig. 2G**). This hypothesis  
134 is supported by several studies which showed that response onsets (i.e., latency to first AP) of deep layer

135 neurons can rival, and even precede those in layer 4<sup>7, 10, 19</sup>. To quantitatively test this hypothesis, we  
136 measured the additional path length between the border stratum and layer 4 that APs need to travel along  
137 VPM axons. Combined with conduction velocity measurements<sup>20</sup>, the analysis predicted that sensory-  
138 evoked excitation reaches the border stratum 2 to 5 ms ( $3.0 \pm 1.7$  ms) earlier than layer 4 (**Fig. 3A**).

139

140 To test the prediction, we recorded and labeled excitatory neurons across all layers of wS1 in  
141 anesthetized rats. These experiments allowed to precisely control the stimulus onset by deflecting  
142 individual whiskers with a piezoelectric bimorph<sup>10</sup>, and to recover the morphological cell type of the  
143 recorded neurons (**Fig. 3B**). We found that responses in the deep layers to deflections of the whisker  
144 that was somatotopically aligned with the recording site – the principal whisker – were largely restricted  
145 to the populations of border stratum and pyramidal tract neurons (**Fig. S3**). Similar to the multi-whisker  
146 stimulations by airpuff, single whisker deflections evoked AP responses that were more reliable in border  
147 stratum cells when compared to layer 4 neurons (**Fig. 3C**). Response onsets of border stratum cells  
148 (median/25<sup>th</sup>/75<sup>th</sup> percentile: 11.2/10.3/12.4 ms) preceded those in all other excitatory cell types –  
149 including layer 4 – matching the path length-based delay predictions (14.3/13.3/18.4 ms; two-sided Mann-  
150 Whitney U-test: difference: -3.3, 95% CI [-4.0, -2.6],  $U = 1096$ ,  $p < 10^{-10}$ ).

151

152 We further tested the delay predictions by simultaneously recording AP responses in layer 4 and upper  
153 layer 6 of head-fixed, behaving rats. We implanted linear silicon probes with equally-spaced electrodes  
154 that spanned across the depth of wS1. This allowed to record the AP activity of several single units during  
155 awake conditions, and to determine the units' respective depth locations with  $\pm 50$   $\mu\text{m}$  precision. When  
156 animals explored their environment by rhythmically moving the principal whisker – all other whiskers were  
157 trimmed – sensory input was provided by whisker contact with a pole that was placed within range. AP  
158 responses in upper layer 6 preceded those in layer 4 of the same animal (**Fig. 3D**). Across animals, the  
159 average AP onset in layer 4 was hence significantly delayed compared to layer 6 (Kolmogorov-Smirnov  
160 two-sample test:  $D_{60,40} = 0.425$ ,  $p < 0.01$ ), on average by 4 ms (**Fig. 3E**). Our data reveal that inputs from  
161 primary thalamic axons can reliably drive fast APs in border stratum cells, providing the functional basis  
162 of a deep thalamorecipient pathway for sensory-evoked signal flow.

163

### 164 **Manipulating border stratum cells affects broad tuning of cortical output**

165 For the present conditions of single whisker deflections in anesthetized rats, AP responses of pyramidal  
166 tract neurons occurred near simultaneous with those in layer 4, and hence consistently later than in  
167 border stratum cells – approximately 3-4 ms (14.3/13.6/16.2 ms). One of the functions of the border  
168 stratum pathway could thus be that it is involved in driving cortical output patterns, whose onsets thereby

169 rival those in layer 4. In further supported of this hypothesis is the characteristic property of pyramidal  
170 tract neurons to respond to a broader range of stimuli compared to their thalamocortical input neurons <sup>21</sup>.  
171 In case of wS1, pyramidal tract neurons can respond similarly fast to stimulations of several whiskers <sup>22</sup>,  
172 even if their dendrites are located hundreds of micrometers away from the terminal fields of those VPM  
173 axons that provide the respective thalamocortical input <sup>23</sup>. The extensive horizontally projecting axons in  
174 the deep layers, in combination with the earliest and reliable AP responses, hence render border stratum  
175 cells as ideal candidates that could contribute to the fast onsets and broadly tuned characteristics of  
176 cortical output patterns.

177

178 To test this hypothesis, we combined pharmacological injections of the GABA<sub>A</sub> agonist muscimol with  
179 cell-attached recordings in anesthetized rats (**Fig. 4A**). Injection pipettes were positioned at the layer 5/6  
180 border of wS1 by quantifying local field potentials (LFPs) at different cortical depths (**Fig. S4**). The LFP  
181 recordings allowed mapping of the principal whisker that corresponded to the location of the injection site  
182 <sup>24</sup> – here referred to as the ‘manipulated whisker’. Cell-attached recordings were performed in layer 5,  
183 approximately 1 millimeter away from the injection site. This distance assured that axons from border  
184 stratum cells, but not from other cell types that are affected by the pharmacology, overlap with the  
185 recording site (**Fig. 4B**). Pyramidal tract neurons were identified as those that responded to deflections  
186 of several individual whiskers <sup>22</sup> – including the manipulated whisker (**Fig. 4C**). After muscimol injections,  
187 fast responses evoked by the manipulated whisker were abolished in any of the recorded neurons (**Fig.**  
188 **4D**). In contrast, whiskers that were not somatotopically aligned with the injection site (e.g. the principal  
189 whisker at the recording site) maintained their ability to evoke reliable and fast AP responses (**Fig. 4E**).

190

### 191 **Border stratum cells provide an on-switch for cortical output**

192 The pharmacological manipulations suggest that border stratum cells are necessary to drive the fast  
193 component of broadly tuned responses in pyramidal tract neurons. However, the high degree of  
194 recurrence in cortical networks, as well as non-linear mechanisms of synaptic and/or dendritic integration,  
195 pose a general challenge to infer causality between manipulations and the resultant alterations of  
196 neuronal AP responses. To address these issues, we developed a model that allows performing  
197 simulations that mimic the specific conditions of our *in vivo* pharmacology experiments at synaptic,  
198 cellular, and network levels, in the following referred to as *in silico* experiments. A link to download the  
199 model and simulation routines, and a detailed description and validation of all parameters, is provided in  
200 the **SI**. In brief, we embedded the morphology of an *in vivo* labeled pyramidal tract neuron into a previously  
201 reported anatomically realistic network model of rat wS1 <sup>25</sup>. The embedding provided structural  
202 constraints about which neurons, depending on their respective cell type and location within VPM and

203 wS1 (i.e., neurons represent *in vivo* labeled morphologies), can in principle form synaptic connections  
204 with the pyramidal tract neuron (**Fig. 5A**), and where along its dendrites (**Fig. 5B**). Combining the network  
205 model with cell type-specific AP measurements – acquired during conditions that were consistent with  
206 those of our pharmacology experiments<sup>10, 23, 26</sup> – provided functional constraints about which of the  
207 structurally possible connections can in principle provide input to the pyramidal tract neuron, depending  
208 on the identity of the stimulated whisker. We generated 1,800 of such structurally and functionally  
209 plausible synaptic input patterns for each of the 24 major facial whiskers, including those that correspond  
210 to the manipulated and principal whisker of our *in vivo* experiments (**Fig. 5C**). Finally, we converted the  
211 pyramidal tract neuron into a multi-compartmental model (**Fig. S5**), equipped with biophysical properties  
212 at the soma, dendrites, axon initial segment, and synapses that capture the characteristic intrinsic  
213 physiology of this cell type<sup>27</sup>.

214

215 This multi-scale model allowed simulating how the dendrites of pyramidal tract neurons integrate and  
216 transform whisker-specific synaptic input patterns into AP output at the soma (**Movie S1**). The simulations  
217 predicted responses that were indistinguishable from those recorded in pyramidal tract neurons *in vivo*  
218 (**Fig. 5D**). In particular, AP probabilities and onsets in response to both, the principal and manipulated  
219 whisker, were in line with the respective *in vivo* data (**Fig. 5E**). We hence performed pharmacology  
220 experiments *in silico*, at a level of spatial and cell type specificity that cannot be achieved *in vivo*.  
221 Deactivating only the border stratum cells within a volume that corresponds approximately to the spread  
222 of muscimol<sup>7</sup> abolished *in silico* responses to the manipulated whisker, but not to any other whisker (**Fig.**  
223 **5F**). Deactivating all neurons that may be affected by the muscimol, except for the border stratum cells,  
224 had in contrast no impact on the fast component of the simulated activity patterns. Deactivating all border  
225 stratum cells throughout wS1 predicted that pyramidal tract neurons lose their broadly tuned onset  
226 responses. However, the remaining direct input from the VPM is predicted to be still sufficient to evoke  
227 principal whisker responses, but with substantially reduced AP probabilities and later onsets. Our *in vivo*  
228 and *in silico* manipulations reveal that border stratum cells amplify the direct thalamocortical input of  
229 pyramidal tract neurons (**Fig. 5G**), and relay sensory-evoked excitation from the local thalamorecipient  
230 volume to neurons across wS1, thereby driving the fast onsets of broadly tuned cortical output patterns.

231

232 We investigated which of the synaptic input parameters, or parameter combinations, of the multi-scale  
233 model could in general account for the fast onsets of sensory-evoked AP responses in pyramidal tract  
234 neurons. For each simulation trial we quantified the number of synapses that were active during the 25  
235 ms following the stimulus onset, their respective path length distances to the soma, and times of activation  
236 at 1 ms resolution. A principal component analysis of these synaptic input statistics revealed that

237 simulation trials with and without fast AP responses formed systematically different distributions with  
238 respect to PC<sub>1</sub> (**Fig. 6A**). 92% of the separation along the dimension of PC<sub>1</sub> could be attributed to a single  
239 quantity (**Fig. 6B**), in the following referred to as synchronous proximal drive (SPD). SPD represents two  
240 effective parameters: the number and synchrony of active excitatory synapses that impinge onto the  
241 proximal dendrites (i.e., path length distance to the soma < 500 μm). SPD was an almost perfect predictor  
242 (**Fig. 6C**) for AP responses (i.e., area under the receiver operating curve (AUROC) equals 1) during  
243 simulations of passive whisker deflections (AUROC = 0.83±0.03). Simulations in which we systematically  
244 varied these two parameters hence provided general relationships between the number of proximal  
245 inputs that are active within a certain time window and the resultant probability of AP responses in  
246 pyramidal tract neurons (**Fig. 6D**). Supporting the manipulation results, these simulations predicted that  
247 – for the present experimental conditions – only combined input from the VPM and border stratum cells  
248 would be sufficiently numerous and synchronous to drive the fast APs at response probabilities which  
249 match with those observed for PW, SW and MW deflections *in vivo*.

250

## 251 Discussion

252 We provide several lines of structural, functional, and computational evidence, which reveal the logic of  
253 bistratified thalamocortical input to rat wS1: preceding the vertical stream of sensory-evoked signal flow  
254 from layer 4 to layers 2/3, the strategically placed border stratum cells give rise to a second stream of  
255 excitation that spreads horizontally across layers 5/6. Parallel activation of layer 4 and a deep input  
256 stratum is likely to generalize to other sensory systems and species. For example in macaque V1,  
257 neurons – sometimes referred to as Meynert cells – have been described whose features are reminiscent  
258 of those that characterize the border stratum cells: they cluster around the layer 5/6 border and have  
259 extensive horizontal axons that span across the deep layers<sup>4</sup>. The function of Meynert cells remains  
260 unknown<sup>28</sup>. However, because of strong similarities in receptive field shapes between neurons in layers  
261 4 and 6, it was suggested that these cells might be strategically placed to receive thalamocortical input  
262 from the deep layer terminal fields of lateral geniculate nucleus (LGN) axons<sup>4</sup>. It was even speculated  
263 that strong thalamocortical input to horizontally projecting neurons in the deep layers represents an  
264 organizational principle that is unique to primates, and which may underlie their superior cognitive  
265 capabilities<sup>28</sup>. However, bistratified LGN axons, as well as horizontally projecting thalamorecipient  
266 corticocortical neurons in the deep layers were also reported for V1 in cats<sup>5, 29</sup> and rodents<sup>16</sup>.

267

268 We showed that the horizontal stream of excitation is necessary – and can even be sufficient – to drive  
269 fast sensory-evoked APs in pyramidal tract neurons. Bypassing the intracortical circuitry of the upper  
270 layers, the deep input stratum hence allows pyramidal tract neurons to integrate and transform sensory



271 inputs from differently tuned thalamocortical populations into cortical output, which can thereby contain  
272 the entire stimulus information that was simultaneously provided by the thalamus (e.g. multi-whisker<sup>30</sup> or  
273 binocular<sup>31</sup> stimuli in wS1 or V1). In addition to providing subcortical circuits with such an integrated  
274 efference copy of the sensory input<sup>32</sup>, the fast activation of pyramidal tract neurons will also be critical  
275 for intracortical computations. Somatic APs back-propagate into the apical dendrites, triggering the  
276 activation of calcium channels<sup>33</sup> that widen the pyramidal tract neurons' time window for synaptic  
277 integration<sup>34</sup>. The fast back-propagating APs that are driven by the border stratum cells will therefore  
278 switch the dendrites of pyramidal tract neurons into an active state, which occurs near simultaneous with  
279 responses in layer 4 that are driven directly by the thalamus. The two input strata could hence  
280 complement each other, ensuring that pyramidal tract neurons are able to reliably transform inputs from  
281 recurrent intracortical circuits – e.g. those from layers 2/3 that are driven by layer 4 – into cortical output  
282<sup>35</sup>. This theory is not only in line with the recent observation that sensory-evoked calcium transients in  
283 apical dendrites of pyramidal tract neurons correlate with perceptual thresholds during whisker-based  
284 behaviors<sup>36</sup>. It further provides a potential explanation for the origin of sustained AP responses in  
285 pyramidal tract neurons<sup>14</sup> that persist for the duration of the stimulus (**Fig. S6**).

286

287 The deep input stratum will be involved in other functions, beyond regulating cortical output patterns.  
288 Axons of border stratum cells innervate all layers of wS1, but in particular layer 4. The fast and reliable  
289 activation of these neurons may therefore contribute to the substantial intracortical component of sensory-  
290 evoked post-synaptic potentials in the major thalamorecipient layer<sup>37</sup>. Moreover, at least a subset of the  
291 border stratum cells display long-range intrinsic axons that innervate higher-order cortices<sup>38</sup>, a property  
292 that they share also with the Meynert cells<sup>39</sup>. Revealing how activity patterns can be coordinated across  
293 intracortical and subcortical circuits, the parallel strata principle provides insight that will be essential for  
294 understanding how the neocortex orchestrates sensory-guided behaviors.

295

## 296 **Acknowledgements**

297 We thank Bert Sakmann for discussions; Etay Hay and Idan Segev for providing biophysical models and  
298 optimization routines; Martin Schwarz for providing the AAV; Idan Segev, David Fitzpatrick and Kevan  
299 Martin for comments on the manuscript. Funding was provided by the European Research Council under  
300 the European Union's Horizon 2020 research and innovation program (No 633428), and in part by the  
301 German Federal Ministry of Education and Research Grants BMBF/FKZ 01GQ1002 and 01IS18052, and  
302 the Deutsche Forschungsgemeinschaft (SFB 1089). **We declare that we have no conflicting interests.**

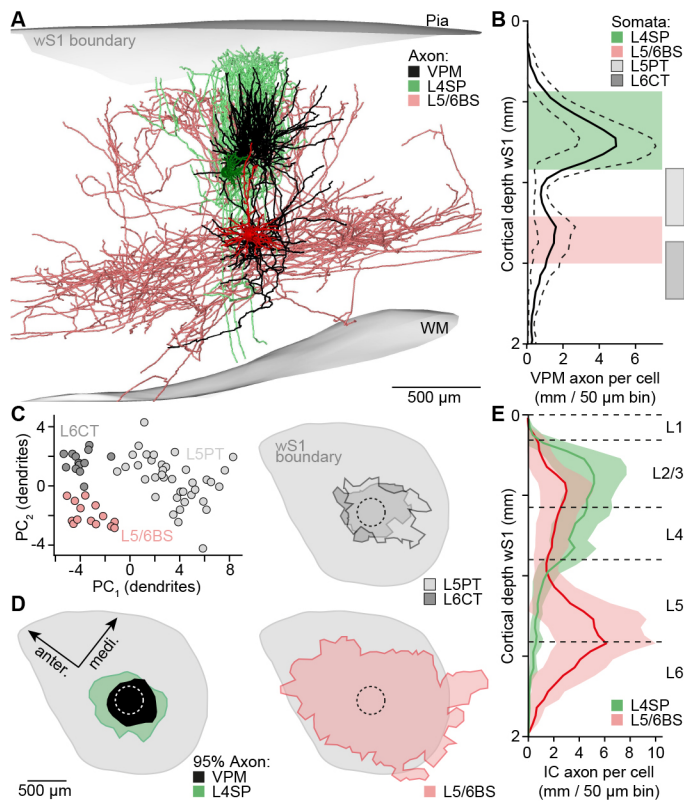
303

304 **Author contributions**

305 M.O. conceived and designed the study. R.E. developed the model and performed simulations. R.N.  
 306 performed cell-attached recordings, pharmacology experiments, and morphological reconstructions. D.U.  
 307 developed analysis and data acquisition routines. A.B. performed simulations. J.G. performed virus  
 308 injections and cell-attached recordings. S.D. performed extracellular recordings. C.K. performed cell-  
 309 attached and extracellular recordings. All authors analyzed data. M.O. wrote the paper.

310

311 **Figures and Figure Legends**

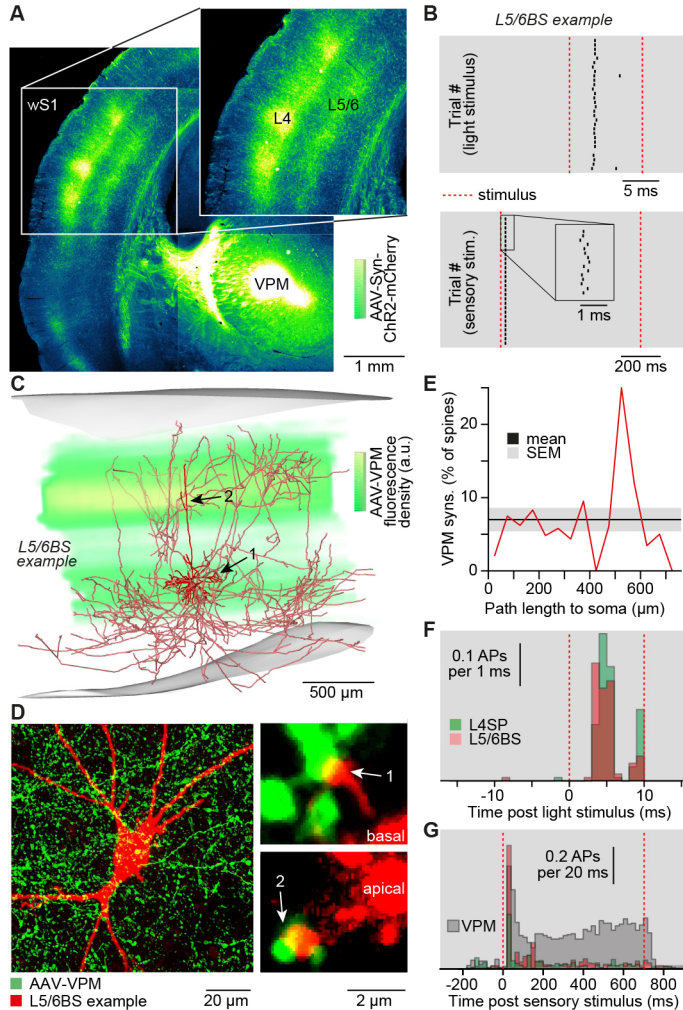


312

313 **Figure 1: Structural basis of two thalamocortical input strata. A)** Examples of *in vivo* labeled neurons  
 314 in the whisker-related part of rat primary somatosensory cortex (wS1): layer 4 spiny neuron (L4SP),  
 315 corticocortical neuron at the L5/6 border stratum (L5/6BS), and the intracortical (IC) part of the axon from  
 316 a relay cell in the ventral posterior medial nucleus of the thalamus (VPM). **B)** Soma, dendrite and axon  
 317 distributions of individual neurons (n=191) were compared with 50 μm precision<sup>9</sup>. Somata of L4SP (n=37)  
 318 and L5/6BS cells (n=14) cluster around the two innervation peaks of VPM axons (n=14, mean ± STD).  
 319 Somata of L5/6BS cells intermingle with those of the subcortically projecting pyramidal tract (L5PT, n=38)  
 320 and corticothalamic (L6CT, n=13) neurons. **C)** Principal components (PC<sub>1/2</sub>) of dendritic features that  
 321 discriminate between excitatory cell types in the deep layers<sup>12, 13</sup> (representing the cells in panel B). **D)**

322 Horizontal axon extent (95% iso-contours) of VPM (n=14), L4SP (n=14), L5PT (n=7), L6CT (n=11) and  
 323 L5/6BS (n=9) neurons. Top views onto wS1. **E**) Vertical distributions of L4SP and L5/6BS axons (same  
 324 cells as in panel D) vs. cytoarchitectonic layer borders <sup>11</sup>.

325

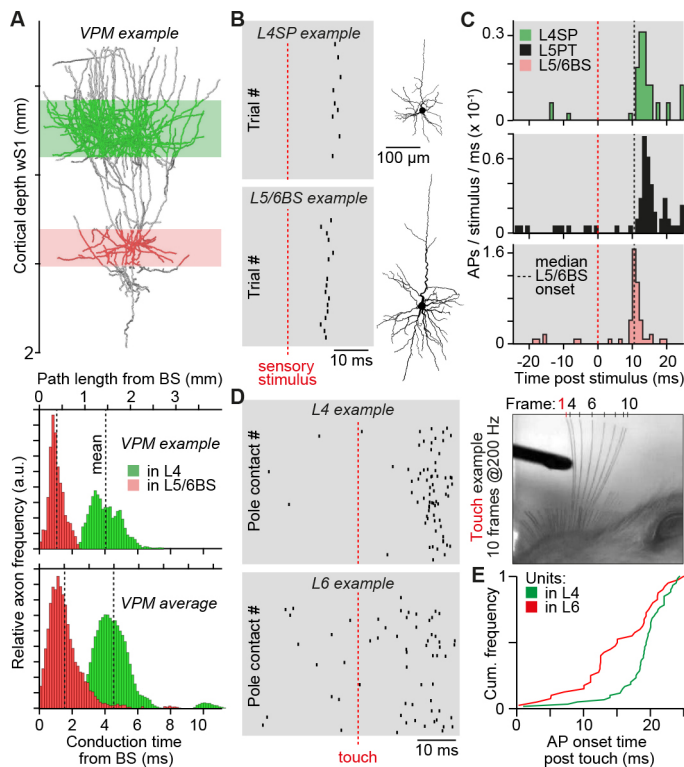


326

327 **Figure 2: Synaptic basis of two thalamocortical input strata. A)** Coronal brain section (50  $\mu$ m) after  
 328 injection of an adeno-associated virus (AAV) into the VPM, which expresses channel rhodopsin (ChR2)  
 329 and a fluorescent marker (mCherry) in thalamocortical (TC) synapses. **B)** Example of cell-attached *in*  
 330 *in vivo* recording in wS1 of AAV-injected brain. Ticks represent APs in response to a 10 ms flash of green  
 331 light onto the cortical surface (upper panel), and a 700 ms airpuff onto the whiskers (lower panel). **C)**  
 332 Reconstruction of the L5/6BS cell shown in panel B, superimposed with quantification of AAV labeling.  
 333 **D)** Confocal images of the L5/6BS cell shown in panel C. Putative TC synapses were identified as  
 334 contacts between VPM boutons and dendritic spines. **E)** Fraction of spines (n=4789) along the dendrites  
 335 of the L5/6BS cell shown in panel B-D that are contacted by VPM boutons. **F)** Post-stimulus-time-  
 336 histograms (PSTHs) of light-evoked APs in L4SP and L5/6BS cells (mean  $\pm$  STD of AP onset:  $4.6 \pm 0.7$

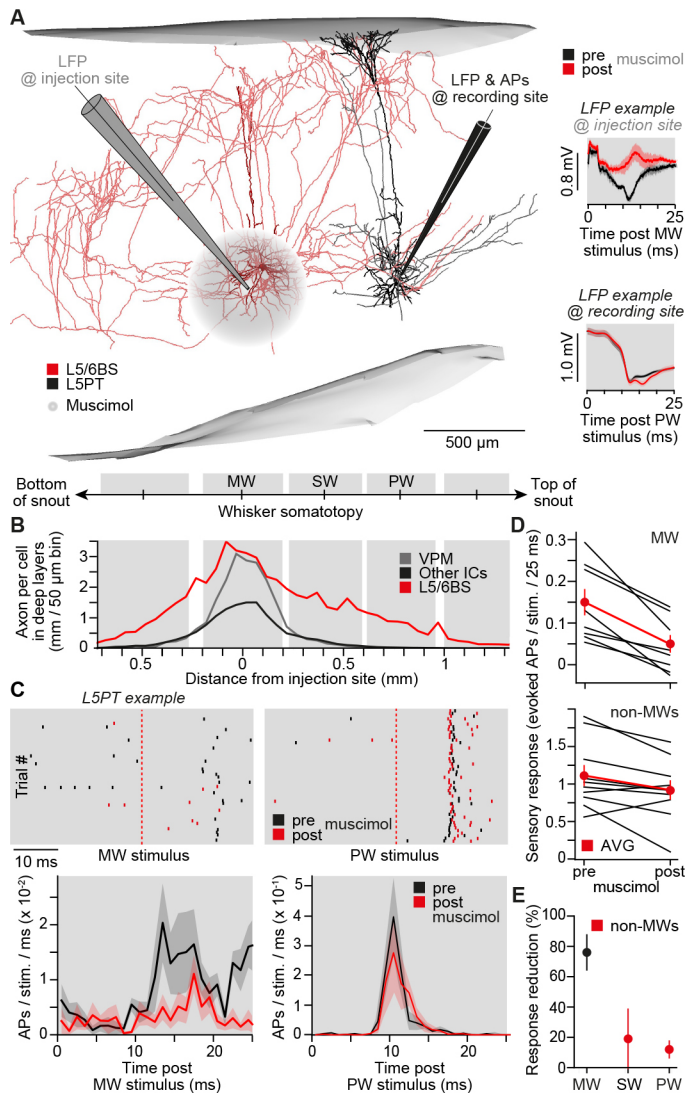
337 ms,  $n=4$  vs.  $4.4 \pm 0.8$  ms,  $n=4$ ). **G**) PSTHs of airpuff-evoked APs in L4SP, L5/6BS (same cells as in panel  
 338 F) and VPM cells ( $n=7$ ).

339



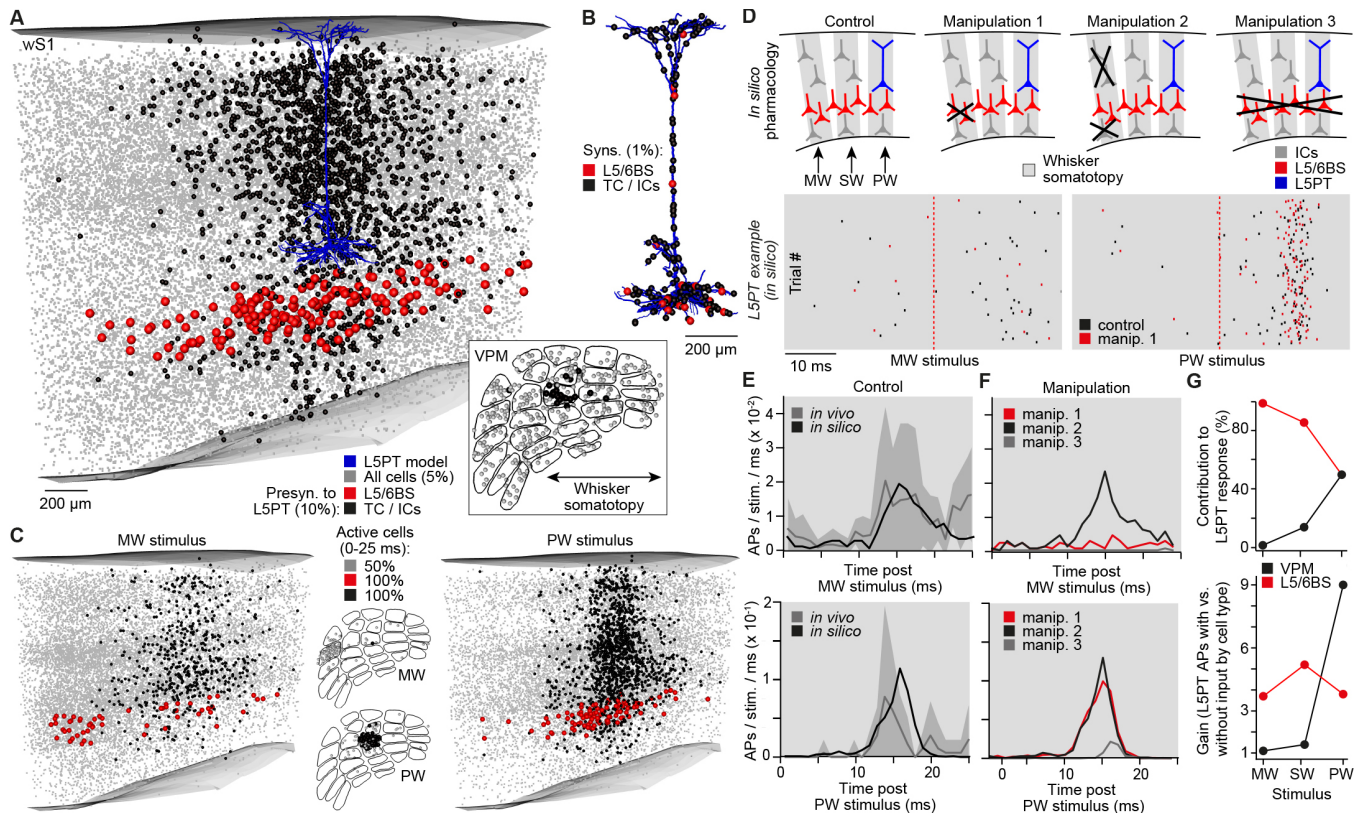
340

341 **Figure 3: Functional basis of two thalamocortical input strata. A)** Example of *in vivo* labeled VPM  
 342 axon (upper panel), whose path length distribution was quantified with respect to the deepest location of  
 343 the border stratum (L5/6BS), and multiplied with the IC conduction velocity ( $0.33 \text{ m/s}^{20}$ ) of TC axons  
 344 (center panel). Average conduction time of VPM axons ( $n=14$ ) to the border stratum and layer 4 (lower  
 345 panel). **B)** AP responses evoked by principal whisker (PW) deflections in exemplary L4SP and L5/6BS  
 346 cells. **C)** PSTHs of PW-evoked APs in morphologically identified L4SP ( $n=8$ ), L5PT ( $n=9$ ) and L5/6BS  
 347 ( $n=6$ ) cells. **D)** Example of simultaneously recorded single units in layer 4 and upper layer 6 ( $\sim 1.6$  mm  
 348 recording depth), which show reliable AP responses after PW contact with a pole during exploratory  
 349 whisking (right panel: whisker positions after exemplary touch). **E)** Distribution of touch-evoked AP onsets  
 350 across animals ( $n=3$ ) in layer 4 and upper layer 6.



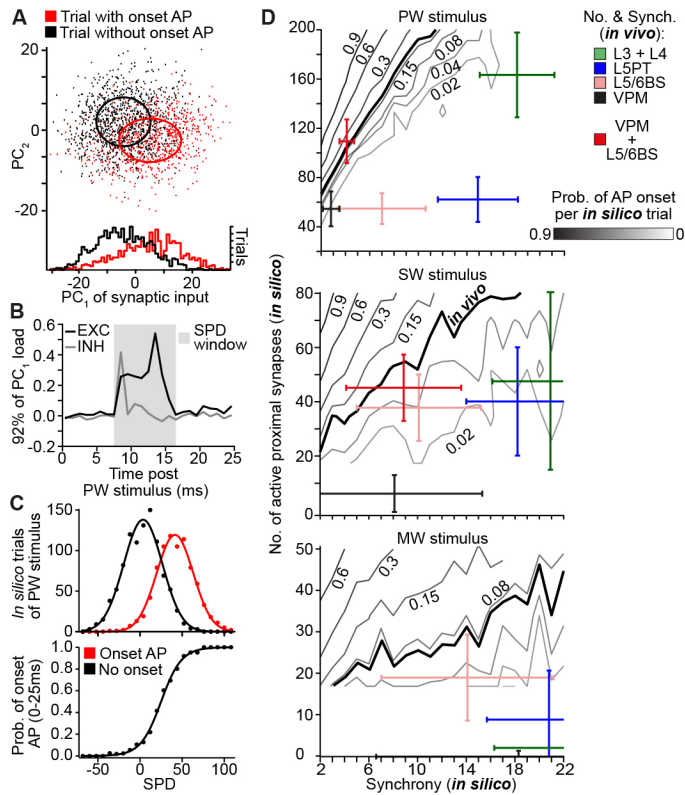
351

352 **Figure 4: Onsets of broadly tuned cortical output patterns are driven by L5/6BS cells.** **A)** The  
 353 somatotopy of rat wS1<sup>9</sup> in combination with whisker-evoked local field potential (LFP) measurements<sup>24</sup>,  
 354 allowed placing of muscimol injection and recording pipettes such that the respective PWs were  
 355 separated by one whisker. Here the PW at the recording site is B2, the manipulated whisker (MW) is D2,  
 356 and the separating whisker (SW) is C2. Left panel: L5/6BS and L5PT cells labeled in the same animal  
 357 illustrate pharmacology experiments. Right panels: example LFPs before and after muscimol injections.  
 358 **B)** Axonal extent in the deep layers from neurons-MWs located in the barrel column that represents the MW.  
 359 **C)** Exemplary AP responses evoked by MW and PW deflections and PSTHs across cells (mean  $\pm$  SEM;  
 360 MW: n=8, PW: n=5). **D)** Response per cell to deflections of the MW (n=8, Wilcoxon rank-sum test: median  
 361 = 0.095, 95% CI [0.05, 0.16], W=36, p=0.008) and non-MWs (PW & SW, n=5 & 5, Wilcoxon rank-sum  
 362 test: median = 0.18, 95% CI [6x10<sup>-5</sup>, 0.38], W=47.5, p=0.05) before and after muscimol injections. Mean  
 363  $\pm$  SEM. **E)** Effect of muscimol on L5PT responses to deflections of the MW and non-MWs.



364

365 **Figure 5: L5/6BS cells amplify and horizontally relay TC inputs to drive L5PT neurons. A)** Example  
 366 distribution of TC (i.e., inset represents model of VPM with barreloids) and IC neurons that provide  
 367 synaptic input to a multi-compartmental L5PT model, embedded into an anatomically realistic model of  
 368 rat wS1<sup>25</sup>. **B)** Synapse locations along the dendrites of the L5PT model corresponding to the distribution  
 369 of input neurons in panel A. **C)** Example distributions of VPM and IC neurons that provide synaptic input  
 370 to the L5PT model during simulations of MW or PW deflections. **D)** Dendritic integration of such generated  
 371 synaptic input patterns (i.e., for deflections of the MW, SW and PW, respectively) and transformation into  
 372 somatic APs were simulated for four different (pharmacology) scenarios. Raster plots represent APs of  
 373 the L5PT model for 200 of these input patterns, respectively. **E)** PSTHs predicted by the L5PT model for  
 374 (control scenario) and as measured *in vivo* for deflections of the PW (n=9) and MW (n=8). **F)** PSTHs  
 375 predicted by the L5PT model for the three different manipulation scenarios. **G)** Relative fractions of VPM  
 376 and L5/6BS synapses that provided input to the L5PT model during simulations of MW, SW and PW  
 377 deflections (upper panel), and the respective amplifications of L5PT AP responses (lower panel).



378

379 **Figure 6: L5/6BS cells provide synchronous drive to proximal dendrites of L5PT neurons.**

380 **A.** PC analysis of spatiotemporal synaptic inputs that impinge onto the L5PT model during simulations of  
 381 PW deflections. **B.** 92% of the separation between simulation trials with and without fast AP responses  
 382 are reflected by PC<sub>1</sub>, which represents the net excitatory input to proximal dendrites within a time window  
 383 of 8-16 ms. These two parameters are combined into a single quantity: synchronous proximal drive  
 384 (SPD). **C.** SPD is an almost perfect predictor for AP responses during simulations of the L5PT model. **D.**  
 385 Probabilities of fast AP responses after simulations of PW, SW and MW deflections as predicted for  
 386 different combinations of the number and synchrony of proximal inputs vs. cell type-specific data derived  
 387 from empirical constraints of the model. Bold lines represent our *in vivo* measurements.

388

## 389 References

- 390 1. Bruno RM, Sakmann B. Cortex is driven by weak but synchronously active thalamocortical  
 391 synapses. *Science* **312**, 1622-1627 (2006).  
 392 2. Harris KD, Shepherd GM. The neocortical circuit: themes and variations. *Nat Neurosci* **18**, 170-  
 393 181 (2015).  
 394 3. Douglas RJ, Martin KA. Neuronal circuits of the neocortex. *Annu Rev Neurosci* **27**, 419-451  
 395 (2004).  
 396 4. Lund JS. Anatomical organization of macaque monkey striate visual cortex. *Annu Rev Neurosci*  
 397 **11**, 253-288 (1988).  
 398 5. Antonini A, Stryker MP. Rapid remodeling of axonal arbors in the visual cortex. *Science* **260**,  
 399 1819-1821 (1993).

- 400 6. Oberlaender M, Ramirez A, Bruno RM. Sensory experience restructures thalamocortical axons  
401 during adulthood. *Neuron* **74**, 648-655 (2012).
- 402 7. Constantinople CM, Bruno RM. Deep cortical layers are activated directly by thalamus. *Science*  
403 **340**, 1591-1594 (2013).
- 404 8. Feldmeyer D, *et al.* Barrel cortex function. *Prog Neurobiol* **103**, 3-27 (2013).
- 405 9. Egger R, Narayanan RT, Helmstaedter M, de Kock CP, Oberlaender M. 3D reconstruction and  
406 standardization of the rat vibrissal cortex for precise registration of single neuron morphology.  
407 *PLoS Comput Biol* **8**, e1002837 (2012).
- 408 10. de Kock CP, Bruno RM, Spors H, Sakmann B. Layer- and cell-type-specific suprathreshold  
409 stimulus representation in rat primary somatosensory cortex. *J Physiol* **581**, 139-154 (2007).
- 410 11. Meyer HS, Egger R, Guest JM, Foerster R, Reissl S, Oberlaender M. Cellular organization of  
411 cortical barrel columns is whisker-specific. *Proc Natl Acad Sci U S A* **110**, 19113-19118 (2013).
- 412 12. Narayanan RT, *et al.* Beyond Columnar Organization: Cell Type- and Target Layer-Specific  
413 Principles of Horizontal Axon Projection Patterns in Rat Vibrissal Cortex. *Cereb Cortex* **25**, 4450-  
414 4468 (2015).
- 415 13. Oberlaender M, *et al.* Cell type-specific three-dimensional structure of thalamocortical circuits in  
416 a column of rat vibrissal cortex. *Cereb Cortex* **22**, 2375-2391 (2012).
- 417 14. Rojas-Piloni G, Guest JM, Egger R, Johnson AS, Sakmann B, Oberlaender M. Relationships  
418 between structure, in vivo function and long-range axonal target of cortical pyramidal tract  
419 neurons. *Nat Commun* **8**, 870 (2017).
- 420 15. Crandall SR, Patrick SL, Cruikshank SJ, Connors BW. Infrabarrels Are Layer 6 Circuit Modules  
421 in the Barrel Cortex that Link Long-Range Inputs and Outputs. *Cell Rep* **21**, 3065-3078 (2017).
- 422 16. Velez-Fort M, *et al.* The stimulus selectivity and connectivity of layer six principal cells reveals  
423 cortical microcircuits underlying visual processing. *Neuron* **83**, 1431-1443 (2014).
- 424 17. Schoonover CE, *et al.* Comparative strength and dendritic organization of thalamocortical and  
425 corticocortical synapses onto excitatory layer 4 neurons. *J Neurosci* **34**, 6746-6758 (2014).
- 426 18. Kumar P, Ohana O. Inter- and intralaminar subcircuits of excitatory and inhibitory neurons in layer  
427 6a of the rat barrel cortex. *J Neurophysiol* **100**, 1909-1922 (2008).
- 428 19. O'Connor DH, Peron SP, Huber D, Svoboda K. Neural activity in barrel cortex underlying vibrissa-  
429 based object localization in mice. *Neuron* **67**, 1048-1061 (2010).
- 430 20. Salami M, Itami C, Tsumoto T, Kimura F. Change of conduction velocity by regional myelination  
431 yields constant latency irrespective of distance between thalamus and cortex. *Proc Natl Acad Sci*  
432 *U S A* **100**, 6174-6179 (2003).
- 433 21. Wright N, Fox K. Origins of cortical layer V surround receptive fields in the rat barrel cortex. *J*  
434 *Neurophysiol* **103**, 709-724 (2010).
- 435 22. Manns ID, Sakmann B, Brecht M. Sub- and suprathreshold receptive field properties of pyramidal  
436 neurones in layers 5A and 5B of rat somatosensory barrel cortex. *J Physiol* **556**, 601-622 (2004).
- 437 23. Brecht M, Sakmann B. Whisker maps of neuronal subclasses of the rat ventral posterior medial  
438 thalamus, identified by whole-cell voltage recording and morphological reconstruction. *J Physiol*  
439 **538**, 495-515 (2002).
- 440 24. Lee JH, Shin HS, Lee KH, Chung S. LFP-guided targeting of a cortical barrel column for in vivo  
441 two-photon calcium imaging. *Sci Rep* **5**, 15905 (2015).
- 442 25. Egger R, Dercksen VJ, Udvary D, Hege HC, Oberlaender M. Generation of dense statistical  
443 connectomes from sparse morphological data. *Front Neuroanat* **8**, 129 (2014).
- 444 26. Bruno RM, Simons DJ. Feedforward mechanisms of excitatory and inhibitory cortical receptive  
445 fields. *J Neurosci* **22**, 10966-10975 (2002).
- 446 27. Hay E, Hill S, Schurmann F, Markram H, Segev I. Models of neocortical layer 5b pyramidal cells  
447 capturing a wide range of dendritic and perisomatic active properties. *PLoS Comput Biol* **7**,  
448 e1002107 (2011).
- 449 28. Briggs F. Organizing principles of cortical layer 6. *Front Neural Circuits* **4**, 3 (2010).



- 450 29. Karube F, Sari K, Kisvarday ZF. Axon topography of layer 6 spiny cells to orientation map in the  
451 primary visual cortex of the cat (area 18). *Brain Struct Funct* **222**, 1401-1426 (2017).
- 452 30. Ramirez A, Pnevmatikakis EA, Merel J, Paninski L, Miller KD, Bruno RM. Spatiotemporal  
453 receptive fields of barrel cortex revealed by reverse correlation of synaptic input. *Nat Neurosci* **17**,  
454 866-875 (2014).
- 455 31. Li H, Fukuda M, Tanifuji M, Rockland KS. Intrinsic collaterals of layer 6 Meynert cells and  
456 functional columns in primate V1. *Neuroscience* **120**, 1061-1069 (2003).
- 457 32. Sherman SM. Thalamus plays a central role in ongoing cortical functioning. *Nat Neurosci* **19**, 533-  
458 541 (2016).
- 459 33. Markram H, Helm PJ, Sakmann B. Dendritic calcium transients evoked by single back-  
460 propagating action potentials in rat neocortical pyramidal neurons. *J Physiol* **485** ( Pt 1), 1-20  
461 (1995).
- 462 34. Larkum ME, Zhu JJ, Sakmann B. A new cellular mechanism for coupling inputs arriving at different  
463 cortical layers. *Nature* **398**, 338-341 (1999).
- 464 35. Hay E, Segev I. Dendritic Excitability and Gain Control in Recurrent Cortical Microcircuits. *Cereb*  
465 *Cortex* **25**, 3561-3571 (2015).
- 466 36. Takahashi N, Oertner TG, Hegemann P, Larkum ME. Active cortical dendrites modulate  
467 perception. *Science* **354**, 1587-1590 (2016).
- 468 37. Cohen-Kashi Malina K, Mohar B, Rappaport AN, Lampl I. Local and thalamic origins of correlated  
469 ongoing and sensory-evoked cortical activities. *Nat Commun* **7**, 12740 (2016).
- 470 38. Zhang ZW, Deschenes M. Intracortical axonal projections of lamina VI cells of the primary  
471 somatosensory cortex in the rat: a single-cell labeling study. *J Neurosci* **17**, 6365-6379 (1997).
- 472 39. Fries W, Keizer K, Kuypers HG. Large layer VI cells in macaque striate cortex (Meynert cells)  
473 project to both superior colliculus and prestriate visual area V5. *Exp Brain Res* **58**, 613-616 (1985).
- 474

## 475 **Methods and Supplement only**

- 476 40. Narayanan RT, Mohan H, Broersen R, de Haan R, Pieneman AW, de Kock CP. Juxtosomal  
477 biocytin labeling to study the structure-function relationship of individual cortical neurons. *J Vis*  
478 *Exp*, e51359 (2014).
- 479 41. Boudewijns ZS, *et al.* Layer-specific high-frequency action potential spiking in the prefrontal cortex  
480 of awake rats. *Front Cell Neurosci* **7**, 99 (2013).
- 481 42. Clack NG, *et al.* Automated tracking of whiskers in videos of head fixed rodents. *PLoS Comput*  
482 *Biol* **8**, e1002591 (2012).
- 483 43. Siegle JH, Lopez AC, Patel YA, Abramov K, Ohayon S, Voigts J. Open Ephys: an open-source,  
484 plugin-based platform for multichannel electrophysiology. *J Neural Eng* **14**, 045003 (2017).
- 485 44. Rossant C, *et al.* Spike sorting for large, dense electrode arrays. *Nat Neurosci* **19**, 634-641 (2016).
- 486 45. Bartho P, Hirase H, Monconduit L, Zugaro M, Harris KD, Buzsaki G. Characterization of  
487 neocortical principal cells and interneurons by network interactions and extracellular features. *J*  
488 *Neurophysiol* **92**, 600-608 (2004).
- 489 46. Wong-Riley M. Changes in the visual system of monocularly sutured or enucleated cats  
490 demonstrable with cytochrome oxidase histochemistry. *Brain Res* **171**, 11-28 (1979).
- 491 47. Horikawa K, Armstrong WE. A versatile means of intracellular labeling: injection of biocytin and  
492 its detection with avidin conjugates. *J Neurosci Methods* **25**, 1-11 (1988).
- 493 48. Oberlaender M, Bruno RM, Sakmann B, Broser PJ. Transmitted light brightfield mosaic  
494 microscopy for three-dimensional tracing of single neuron morphology. *J Biomed Opt* **12**, 064029  
495 (2007).
- 496 49. Dercksen VJ, Hege HC, Oberlaender M. The Filament Editor: an interactive software environment  
497 for visualization, proof-editing and analysis of 3D neuron morphology. *Neuroinformatics* **12**, 325-  
498 339 (2014).

- 499 50. Mainen ZF, Carnevale NT, Zador AM, Claiborne BJ, Brown TH. Electrotonic architecture of  
500 hippocampal CA1 pyramidal neurons based on three-dimensional reconstructions. *J*  
501 *Neurophysiol* **76**, 1904-1923 (1996).
- 502 51. Druckmann S, Banitt Y, Gidon A, Schurmann F, Markram H, Segev I. A novel multiple objective  
503 optimization framework for constraining conductance-based neuron models by experimental data.  
504 *Front Neurosci* **1**, 7-18 (2007).
- 505 52. Hines ML, Carnevale NT. The NEURON simulation environment. *Neural Comput* **9**, 1179-1209  
506 (1997).
- 507 53. Arzt M, Sakmann B, Meyer HS. Anatomical Correlates of Local, Translaminar, and Transcolumnar  
508 Inhibition by Layer 6 GABAergic Interneurons in Somatosensory Cortex. *Cereb Cortex*, 1-12  
509 (2017).
- 510 54. Helmstaedter M, Sakmann B, Feldmeyer D. L2/3 interneuron groups defined by multiparameter  
511 analysis of axonal projection, dendritic geometry, and electrical excitability. *Cereb Cortex* **19**, 951-  
512 962 (2009).
- 513 55. Koelbl C, Helmstaedter M, Lubke J, Feldmeyer D. A barrel-related interneuron in layer 4 of rat  
514 somatosensory cortex with a high intrabarrel connectivity. *Cereb Cortex* **25**, 713-725 (2015).
- 515 56. Egger R, Schmitt AC, Wallace DJ, Sakmann B, Oberlaender M, Kerr JN. Robustness of sensory-  
516 evoked excitation is increased by inhibitory inputs to distal apical tuft dendrites. *Proc Natl Acad*  
517 *Sci U S A* **112**, 14072-14077 (2015).
- 518 57. Feldmeyer D, Lubke J, Silver RA, Sakmann B. Synaptic connections between layer 4 spiny  
519 neurone-layer 2/3 pyramidal cell pairs in juvenile rat barrel cortex: physiology and anatomy of  
520 interlaminar signalling within a cortical column. *J Physiol* **538**, 803-822 (2002).
- 521 58. Wozny C, Williams SR. Specificity of synaptic connectivity between layer 1 inhibitory interneurons  
522 and layer 2/3 pyramidal neurons in the rat neocortex. *Cereb Cortex* **21**, 1818-1826 (2011).
- 523 59. Jahr CE, Stevens CF. A quantitative description of NMDA receptor-channel kinetic behavior. *J*  
524 *Neurosci* **10**, 1830-1837 (1990).
- 525 60. Larkum ME, Nevian T, Sandler M, Polsky A, Schiller J. Synaptic integration in tuft dendrites of  
526 layer 5 pyramidal neurons: a new unifying principle. *Science* **325**, 756-760 (2009).
- 527 61. Schnepel P, Kumar A, Zohar M, Aertsen A, Boucsein C. Physiology and Impact of Horizontal  
528 Connections in Rat Neocortex. *Cereb Cortex* **25**, 3818-3835 (2015).
- 529 62. Gupta A, Wang Y, Markram H. Organizing principles for a diversity of GABAergic interneurons  
530 and synapses in the neocortex. *Science* **287**, 273-278 (2000).
- 531 63. Petersen CC, Hahn TT, Mehta M, Grinvald A, Sakmann B. Interaction of sensory responses with  
532 spontaneous depolarization in layer 2/3 barrel cortex. *Proc Natl Acad Sci U S A* **100**, 13638-13643  
533 (2003).
- 534 64. Reyes-Puerta V, Sun JJ, Kim S, Kilb W, Luhmann HJ. Laminar and Columnar Structure of  
535 Sensory-Evoked Multineuronal Spike Sequences in Adult Rat Barrel Cortex In Vivo. *Cereb Cortex*  
536 **25**, 2001-2021 (2015).
- 537 65. Lefort S, Tomm C, Floyd Sarria JC, Petersen CC. The excitatory neuronal network of the C2  
538 barrel column in mouse primary somatosensory cortex. *Neuron* **61**, 301-316 (2009).
- 539 66. Thomson AM, West DC, Wang Y, Bannister AP. Synaptic connections and small circuits involving  
540 excitatory and inhibitory neurons in layers 2-5 of adult rat and cat neocortex: triple intracellular  
541 recordings and biocytin labelling in vitro. *Cereb Cortex* **12**, 936-953 (2002).
- 542 67. Brown SP, Hestrin S. Intracortical circuits of pyramidal neurons reflect their long-range axonal  
543 targets. *Nature* **457**, 1133-1136 (2009).
- 544 68. Perin R, Berger TK, Markram H. A synaptic organizing principle for cortical neuronal groups. *Proc*  
545 *Natl Acad Sci U S A* **108**, 5419-5424 (2011).
- 546 69. Song S, Sjöström PJ, Reigl M, Nelson S, Chklovskii DB. Highly nonrandom features of synaptic  
547 connectivity in local cortical circuits. *PLoS Biol* **3**, e88 (2005).
- 548 70. Thomson AM, West DC, Hahn J, Deuchars J. Single axon IPSPs elicited in pyramidal cells by  
549 three classes of interneurons in slices of rat neocortex. *J Physiol* **496 ( Pt 1)**, 81-102 (1996).

## 550 **Methods**

551 **Animal preparation:** All experiments were carried out after evaluation by the local German authorities,  
552 in accordance with the animal welfare guidelines of the Max Planck Society, or with the Dutch law after  
553 evaluation by a local ethical committee at the VU University Amsterdam, The Netherlands.

554

555 **Virus injection:** Male Wistar rats aged 22-25 days (P22-25, m, Charles River) were anesthetized with  
556 isoflurane supplemented by rimadyl (Caprofen, 5mg/ kg) as analgesia, then placed into a stereotaxic  
557 frame (Kopf Instruments, model 1900), and provided with a continuous flow of isoflurane/O<sub>2</sub> gas. Body  
558 temperature was maintained at 37°C by a heating pad. A small craniotomy was made above the left  
559 hemisphere 2.85 mm posterior to bregma and 3.2 mm lateral from the midline. The head of the rat was  
560 leveled with a precision of 1 µm in both the medial-lateral and anterior-posterior planes using an  
561 eLeVeLeR electronic leveling device (Sigmann Electronics, Hüffenhardt, Germany) mounted to an  
562 adapter of the stereotaxic frame. An injecting pipette containing an adeno-associated virus (AAV) was  
563 lowered into the VPM thalamus (5.05 mm from the pia). The virus – rAAV2/1-CAG-hChR2(H134R)-Syn-  
564 mCherry (titer: 1x10<sup>12</sup> gc ml<sup>-1</sup>) – was provided by Martin Schwarz (University of Bonn, Germany). 50-70  
565 nL of the virus were injected using a 30cc syringe coupled to a calibrated glass injection capillary.

566

567 **Cell-attached recording/labeling in virus injected animals:** After a 16-21 day incubation period, AAV  
568 injected rats were anesthetized with urethane (1.8 g/kg body weight) by intraperitoneal injection. The  
569 depth of anesthesia was assessed by monitoring pinch withdrawal, eyelid reflexes, and vibrissae  
570 movements. Body temperature was maintained at 37.5 ± 0.5 °C by a heating pad. Cell-attached recording  
571 and labeling was performed as described in detail previously<sup>40</sup>. Briefly, APs were recorded using an  
572 extracellular loose patch amplifier (ELC-01X, npi electronic GmbH), and digitized using a CED power1401  
573 data acquisition board (CED, Cambridge Electronic Design, Cambridge, UK). APs were recorded before  
574 and during 20-30 trials of caudal multi-whisker deflections by a 700 ms airpuff (10 PSI), delivered through  
575 a 1 mm plastic tube from a distance of 8-10 cm from the whisker pad<sup>14</sup>. Stimulation was repeated at  
576 constant intervals (0.3 Hz). Optical stimulation of ChR2-expressing thalamocortical terminals was  
577 provided by a 200 µm diameter optical fiber (ThorLabs #RJPSF2) coupled to a 470 nm wavelength LED  
578 (ThorLabs M470F3), resulting in an output power of 1 mW. The fiber was positioned approximately 2 mm  
579 above the cortical surface, resulting in a 1-2 mm disc of light above wS1. APs were recorded during 20-  
580 30 trials of 10 ms light pulses, at an inter-stimulus interval of 2.5 s. Following the electrophysiological  
581 measurements, neurons were filled with biocytin. Filling sessions were repeated several times. After 1-2  
582 hours for tracer diffusion, animals were transcardially perfused with 0.9% saline followed by 4%

583 paraformaldehyde (PFA). Brains were removed and post-fixed with 4% PFA for 24 hours, transferred to  
584 0.05 M phosphate buffer (PB) and stored at 4°C.

585

586 **Pharmacological manipulation:** Wistar rats (P28-P35, m, Charles River) were anesthetized with  
587 urethane (1.6-1.7 g/kg body weight) by intraperitoneal injection. As described above, the depth of  
588 anesthesia was monitored, and the animal's body temperature was maintained. An 'L' shaped craniotomy  
589 centered on the coordinate of the barrel column representing the D2 whisker (2.5 mm posterior and 5.5  
590 mm lateral to the bregma) was made without cutting the dura, and extended along the rostro-medial (i.e.,  
591 along the E-row) and caudal axes (i.e., arc 2) for ~1-2 mm, respectively. Locations for muscimol injections  
592 and recordings were determined with long-tapered 'search pipettes' (tip diameter <3 µm and insertion  
593 diameter <50µm). The search pipette was inserted rostral to wS1 and lowered parallel to the midline  
594 while measuring LFPs at different cortical depths, and in response to deflections of different individual  
595 whiskers using a piezoelectric bimorph<sup>24</sup>. Recordings were made using an Axoclamp 2B amplifier (Axon  
596 instruments, Union City, CA, USA), low pass filtered (300 Hz), and digitized using a CED power1401 data  
597 acquisition board (CED, Cambridge Electronic Design, Cambridge, UK). Using the LFP data, we identified  
598 the depth of the L5/6 border and the principal whisker (e.g. E2), and marked this location on the dura with  
599 a surgical pen. Repeating the LFP-guided whisker mapping with a second search pipette that was  
600 inserted approximately parallel to the vertical axis of wS1, we identified layer 5 of the hence appropriate  
601 recording site (i.e., C2 if the injection pipette was located at E2). This location was also marked on the  
602 dura. Pipettes for muscimol injections were prepared with a tip diameter of 8-12 µm. The taper diameter  
603 at the insertion point into the brain was ~125-150 µm. The tip of the pipette was filled with normal rat  
604 ringer (NRR) to avoid muscimol spill upon pipette insertion. The rest of the pipette was filled with 10 mM  
605 muscimol supplemented with 2% biocytin. The injection pipette was positioned at the previously  
606 determined location, the dura was cut open (~500 µm), and the injection pipette was inserted with positive  
607 pressure of 5-10 mbar. Allowing the tissue to adjust for 10-15 minutes, we inserted a recording pipette  
608 (i.e., 1 µm tip diameter, filled with NRR supplemented with 2% biocytin) at the second previously  
609 determined location. Both locations were confirmed by measuring whisker-evoked LFPs. Pyramidal tract  
610 neurons were identified as follows<sup>10, 13, 22</sup>: (1) recording depth between 1000-1600 µm; (2) ongoing AP  
611 rates between ~1-5 Hz; (3) reliable and fast APs (i.e., between 10-20 ms) in response to principal whisker  
612 deflections; (4) reliable and fast APs after deflection of the manipulated whisker. We identified eight  
613 neurons that matched these criteria (recording / injection location: 1x B1/D1, 4x C1/E1, 3x C2/E2).  
614 Whisker deflections of the PW (e.g. C2), one SW (e.g. D2) and the MW (e.g. E2) were performed (i.e.,  
615 50 trials of 200 ms ramp-and-hold stimulus with an amplitude of ~5°, 2 s inter-stimulus interval), and APs  
616 were recorded, while simultaneously measuring the LFP via the injection pipette. Following these

617 measurements (i.e., control data), muscimol was injected by slowly increasing the pressure onto the  
618 injection pipette (80-300 mbar), while monitoring the LFP in response to MW deflections. Once MW-  
619 evoked LFPs were abolished, and the AP activity remained unaffected, the measurements of whisker-  
620 evoked responses were repeated (i.e., at least 50 trials of PW, SW and MW deflections, respectively).

621

622 **Extracellular recordings:** Wistar rats (P33-P70, m) were anesthetized using 1.6 % isoflurane in 0.4 l/h  
623 O<sub>2</sub> + 0.7 l/h NO<sub>2</sub>, supplemented by rimadyl (Caprofen, 5mg/ kg) as analgesia. A craniotomy of 0.5 mm x  
624 0.5 mm was made above wS1 on the left hemisphere, and a head post for fixation was implanted on the  
625 skull. After recovery from surgery, rats were head-fixed two times per day for 2-3 days. Rats quickly  
626 adjusted to the head-fixation, allowing stable recording conditions without the need of body restraint. Rats  
627 were anaesthetized with isoflurane (1.25% in 0.4 l/h O<sub>2</sub> + 0.7 l/h NO<sub>2</sub>), and a 32-channel linear silicon  
628 probe (E32+R-50-S1-L10(NT), Atlas Neuroengineering, Belgium) was inserted into wS1 for extracellular  
629 multi-unit recordings. Prior to recordings, silicon probes were labeled with Dil (Thermo Fisher Scientific,  
630 Waltham, MA, USA). The probe was connected to a unity-gain headstage (Neuralynx, USA), in series  
631 with the Open Ephys data acquisition board equipped with a RHD2132 digital interface chip (Intan  
632 Technologies, Los Angeles, CA, USA). Using the LFP strategy described above, the PW at the recording  
633 site was identified, all other whiskers were trimmed to 5 mm, and the anesthesia was terminated.  
634 Recordings were performed once the animals were fully awake (~25 minutes after the anesthesia was  
635 terminated<sup>41</sup>). Rats were not trained to perform tactile behavior, and behavior was not rewarded. Sensory  
636 input resulted from whisker touch with a pole that was placed within range during periods of exploratory  
637 whisker self-motion. The touch onset was determined by high-speed videography at 200 frames/s  
638 (MotionScope M3 camera, IDT Europe, Belgium). Whisker angle was tracked offline<sup>42</sup>, and episodes of  
639 whisker movements were classified by thresholding average power in whisker angle versus time (1-20  
640 Hz bandpass) using the Matlab spectrogram function. Touch events were detected manually in each  
641 frame. Signals were acquired at a sampling rate of 30 kHz/channel using Open Ephys GUI<sup>43</sup>. To identify  
642 single units, the data were high-pass filtered, and automatically sorted into clusters using Klustakwik<sup>44</sup>.  
643 The clusters were manually post-processed, and only stable and well-isolated single units were  
644 considered for analysis. The average waveforms of all well-isolated single units were used to sub-classify  
645 units<sup>45</sup> as regular spiking vs. fast spiking units (FSUs). FSUs (AP peak-to-trough time <0.5 ms and AP  
646 half-peak time <0.25 ms) were excluded from the analyses. After recordings, rats were anaesthetized  
647 with urethane (>2.0 g/kg) and perfused with 0.9% NaCl followed by 4% paraformaldehyde (PFA).

648

649 **Histology:** For morphological reconstructions, 100 µm thick vibratome sections were cut tangentially to  
650 wS1 (45° angle) ranging from the pial surface to the white matter (WM). Sections were processed for

651 cytochrome-C oxidase staining to visualize barrel contours in layer 4<sup>46</sup>. All sections were treated with  
652 avidin-biotin (ABC) solution, and subsequently neurons were identified using the chromogen 3,3'-  
653 diaminobenzidine tetrahydrochloride (DAB)<sup>47</sup>. All sections were mounted on glass slides, embedded with  
654 Mowiol, and enclosed with a cover slip. In experiments where AAV injections were combined with biocytin  
655 filling, cortex was cut into 45-48 consecutive 50  $\mu$ m thick tangential sections. Sections were treated with  
656 Streptavidin Alexa-488 conjugate (5mg/ml Molecular Probes #S11223) to stain biocytin labeled  
657 morphologies<sup>14</sup>. To enhance the virus labeling, sections were immunolabeled with anti-mCherry  
658 antibody. Sections were permeabilized and blocked in 0.5% Triton x-100 (TX) (Sigma Aldrich #9002-93-  
659 1) in 100 mM PB containing 4% normal goat serum (NGS) (Jackson ImmunoResearch Laboratories  
660 #005-000-121) for 2 hours at room temperature. The primary antibody was diluted 1:500 (Rabbit anti-  
661 mCherry, Invitrogen #PA5-34974) in PB containing 1% NGS for 24 hours at 4°C. The secondary antibody  
662 was diluted (1:500 goat anti-Rabbit IgG Alexa-647 H+L Invitrogen #A21245) and was incubated for 2-3  
663 hours at room temperature in PB containing 3% NGS and 0.3% TX. All sections were mounted on glass  
664 slides, embedded with SlowFade Gold (Invitrogen #S36936) and enclosed with a cover slip. For  
665 extracellular recording experiments, brains were post-fixed in 4% PFA, and tangential vibratome sections  
666 (100  $\mu$ m) were cut and stained for cytochrome-C. An X-Cite 120 Q light-source (Excelitas Technologies  
667 Corp., Waltham, MA, USA) was used to visualize the Dil electrode tract, and only electrode tracks within  
668 the barrel column that represents the PW were selected for analyses. The histology allowed assigning  
669 the recording depth to each electrode (i.e., and hence to each unit) with approximately 100  $\mu$ m precision.

670

671 **Morphological reconstruction:** Neuronal structures were extracted from image stacks using a  
672 previously reported automated tracing software<sup>48</sup>. 3D image stacks of up to 5 mm  $\times$  5 mm  $\times$  0.1 mm  
673 were acquired using an automated brightfield microscope system (BX-51, Olympus, Japan) at a  
674 resolution of 0.092  $\times$  0.092  $\times$  0.5  $\mu$ m per voxel (100 $\times$  magnification, NA 1.4). For reconstruction of  
675 fluorescently labeled neurons, images were acquired using a confocal laser scanning system (Leica  
676 Application Suite Advanced Fluorescence SP5; Leica Microsystems). 3D image stacks of up to 2.5 mm  
677  $\times$  2.5 mm  $\times$  0.05 mm were acquired at a resolution of 0.092  $\times$  0.092  $\times$  0.5  $\mu$ m per voxel (63 $\times$  magnification,  
678 NA 1.3). Manual proof-editing of individual sections, and automated alignment across sections were  
679 performed using custom-designed software<sup>49</sup>. Pia, barrel and WM outlines were manually drawn on low  
680 resolution images (4 $\times$ ). Using these anatomical reference structures, all reconstructed dendrite and axon  
681 morphologies were registered to the D2 barrel column of a standardized 3D reference frame of rat wS1  
682<sup>9</sup>. The shortest distance from the pial surface to the soma, and 20 morphological features that have  
683 previously been shown to separate between excitatory cell types in rat wS1<sup>9</sup> were calculated for each  
684 reconstructed and registered dendrite morphology. For identification of putative thalamocortical

685 synapses, biocytin labeled morphologies and AAV labeled VPM terminals were imaged simultaneously  
686 using the confocal laser scanning system as described above: biocytin Alexa-488 (excited at 488 nm,  
687 emission detection range 495-550 nm), AAV Alexa-647 (excited at 633 nm, emission detection range  
688 650-785 nm). These dual-channel 3D image stacks were loaded into Amira visualization software (FEI).  
689 All reconstructed dendrites were manually inspected, and landmarks were placed onto each spine head.  
690 If a spine head was overlapping with a VPM bouton, an additional landmark was placed to mark a putative  
691 synapse. The shortest distance of each landmark to the dendrite reconstruction was determined, and the  
692 path length distance was calculated from that location along the reconstructed L5/6BS cell to the soma.

693

694 **Cell type-specific analysis:** In total,  $n=177$  *in vivo* labeled morphologies of excitatory neurons in wS1  
695 (i.e., from urethane anesthetized Wistar rats; P25-P45, m/f, Charles River) were used in this study to  
696 determine cell type-specific whisker receptive fields (wRFs), and to provide structural/functional  
697 constraints for simulation experiments. All morphologies<sup>12, 14</sup> – except for five L5/6BS and one L5PT  
698 neurons – and classification approaches<sup>12, 13</sup>, as well as the corresponding whisker-evoked physiology  
699 data<sup>10, 13</sup> have been reported previously, but in different context. Analysis of wRFs for objectively  
700 classified morphological cell types were not performed for any of the previously reported neurons. Here,  
701 each neuron was objectively assigned to one of the 10 major excitatory cell types of the neocortex<sup>2, 12</sup>  
702 based on the 21 soma-dendritic features described above: three types of pyramids in layers 2-4 (L2PY,  
703 L3PY, L4PY), spiny-stellates (L4ss) and star-pyramids in layer 4 (L4sp), slender-tufted intratelencephalic  
704 (L5IT) and thick-tufted pyramidal tract neurons in layer 5 (L5PTs), polymorphic corticocortical (L6CC) and  
705 corticothalamic neurons in layer 6 (L6CT), and the L5/6 border stratum cells (L5/6BS). In the present  
706 study, we grouped L4ss and L4sp as layer 4 spiny neurons (L4SP). The physiology data (i.e., AP  
707 responses to passive deflections of the principal and its eight adjacent whiskers<sup>10</sup>) were grouped by the  
708 hence determined morphological cell types, resulting cell type-specific wRFs.

709

710 **Multi-compartmental model:** We generated a biophysically-detailed multi-compartmental neuron  
711 model, which captures the stereotypic morphological and intrinsic physiological properties of L5PTs. The  
712 L5PT model is based on the 3D soma-dendrite reconstruction of a L5PT neuron, whose morphological  
713 and topological features – which allow discriminating L5PTs from other excitatory cell types in the deep  
714 layers (see above) – represent approximately the respective averages across a population of 37 L5PTs  
715<sup>12, 14</sup> that were labeled *in vivo* via cell-attached recordings in layer 5 of rat wS1. A simplified axon  
716 morphology was attached to the reconstructed soma based on<sup>50</sup>. The axon consisted of an axon hillock  
717 with a diameter tapering from 3.5  $\mu\text{m}$  to 1  $\mu\text{m}$  over a length of 10  $\mu\text{m}$ , an axon initial segment (AIS) of 10  
718  $\mu\text{m}$  length and 1  $\mu\text{m}$  diameter, and 1 mm of myelinated axon (diameter of 1  $\mu\text{m}$ ). The diameter of the

719 reconstruction of the apical trunk and oblique dendrites was scaled by a factor of 2.5 to allow for  
720 backpropagation of action potentials (bAP), and bAP-triggered calcium spike (BAC) firing to occur (i.e.,  
721 after scaling the diameter of the apical trunk was 4.5  $\mu\text{m}$  at the soma, and 1.5  $\mu\text{m}$  at the main bifurcation  
722 located at a distance of  $\sim 900$   $\mu\text{m}$  from the soma). Spatial discretization of the dendrite morphology (i.e.,  
723 compartmentalization) was performed by computing the electrotonic length constant of each dendrite  
724 branch at a frequency of 100 Hz and setting the length of individual compartments in this branch to 10%  
725 of this length constant. The length of axonal compartments was set to 10  $\mu\text{m}$ . After spatial discretization,  
726 the L5PT morphology consisted of 1033 compartments with an average length of  $\sim 15$   $\mu\text{m}$ , but no longer  
727 than 42  $\mu\text{m}$ . The resultant L5PT model was then combined with previously reported biophysical models  
728 of a variety of Hodgkin-Huxley (HH)-type ion channels (**Table S1**) that are expressed at different densities  
729 within the soma, basal and/or apical dendrites, and axon initial segment <sup>27</sup>. Using an evolutionary multi-  
730 objective optimization algorithm <sup>51</sup>, we tuned the parameters of the biophysical models until numerical  
731 simulations of the L5PT model (using NEURON 7.2 <sup>52</sup>) reproduced current injection-evoked somatic  
732 and/or dendritic sub- and suprathreshold responses that are characteristic for L5PTs, as measured  
733 previously via whole-cell recordings in acute brain slices of rat wS1 *in vitro* <sup>27</sup>. Fixed membrane  
734 parameters were the axial resistance (100  $\Omega\text{cm}$  in all compartments), the membrane capacitance (1  
735  $\mu\text{F}/\text{cm}^2$  at the soma and axon, 2  $\mu\text{F}/\text{cm}^2$  in the apical and basal dendrites to account for increased surface  
736 area due to spines, and 0.04  $\mu\text{F}/\text{cm}^2$  along the myelinated part of the model axon), and the passive  
737 membrane conductance along the myelinated part of the axon ( $g_{\text{pas}} = 0.4$   $\text{pS}/\mu\text{m}^2$ , i.e., equivalent to a  
738 specific membrane resistance of 25,000  $\Omega\text{cm}^2$ ). The reversal potential of the passive membrane  
739 conductance was set to -90 mV. Conductance densities of the non-specific cation current  $I_h$  were fixed at  
740 0.8  $\text{pS}/\mu\text{m}^2$  in the soma and axon, and 2  $\text{pS}/\mu\text{m}^2$  in the basal dendrites. In the apical dendrite, the  
741 conductance density of  $I_h$  increased exponentially with the distance to the soma. The biophysical model  
742 parameters to be optimized were the peak conductance per unit membrane area for various voltage-  
743 dependent ion channels, and the parameters of a phenomenological model of the calcium dynamics in  
744 different parts of the morphology (i.e., axon, soma, basal and apical dendrites; **Table S1**). The targets of  
745 the optimization were different features of the membrane potential in response to two stimuli, as  
746 measured previously <sup>27</sup>: (1) a brief current injection into the soma should trigger an AP at the soma and  
747 a bAP, and (2) a brief current injection into the soma, followed by current injection into a  $\text{Ca}^{2+}$  channel  
748 dense region around the first bifurcation point of the apical tuft, should trigger somatic bursts (i.e., BAC  
749 firing). The specific features, as listed in **Table S2**, were combined into five objectives, which were then  
750 optimized simultaneously by using the evolutionary algorithm <sup>51</sup>. A set of 1,000 models was generated  
751 with parameters drawn randomly from a physiologically plausible range. In every iteration, each model  
752 was then evaluated by simulating the response to the two stimuli, calculating the features and determining



753 the error by calculating the difference between each simulated and measured feature in units of standard  
754 deviations of the experimental feature <sup>27</sup>. After each model had been evaluated, a new set of 1,000  
755 models was generated from the previous set by stochastically transferring parameter values from “good”  
756 models (i.e., lower errors) to “worse” models (i.e., higher errors). Additionally, parameter values of all  
757 models were updated stochastically to avoid converging to local minima. This procedure was repeated  
758 500 times. From the final iteration, the set of biophysical models used here was selected based on three  
759 criteria: (1) it had the lowest sum across all objective errors, (2) similar deviations in all objective errors  
760 (i.e., models where only a subset of objectives matched the experimental data were not considered), and  
761 (3) it supported regular spiking of increasing frequencies in response to sustained current injections of  
762 increasing amplitude.

763

764 **Connectivity model:** The structurally plausible constraints for the numbers and dendritic distributions of  
765 cell type-specific synaptic input patterns that impinge onto the L5PT model are based on an anatomically  
766 realistic network model of rat wS1, as described in detail previously <sup>25</sup>. Briefly, we generated a 3D model  
767 of the average geometry of rat wS1 (i.e., 3D location, orientation and diameter of all barrel columns; 3D  
768 pial and white matter (WM) surfaces), and determined the variability (~50  $\mu\text{m}$ ) of these anatomical  
769 landmarks across twelve animals <sup>9</sup>. Next, we measured the number and 3D distribution of all excitatory  
770 and inhibitory neuron somata in rat wS1 (~530,000 neurons) and the ventral posterior medial nucleus  
771 (VPM) of the thalamus (~6,000 neurons) in four different animals <sup>11</sup>, and generated an average excitatory  
772 and inhibitory 3D neuron somata distribution at a resolution of  $50 \times 50 \times 50 \mu\text{m}^3$ , reflecting the variability of  
773 the cortex geometry across animals. We then registered a sample of 177 excitatory intracortical (IC)  
774 neuron morphologies (i.e., grouped into ten cell types (see above) <sup>10, 12</sup>, 14 excitatory thalamocortical  
775 (TC) axon morphologies labeled in VPM *in vivo* <sup>6</sup>, and the soma-dendrites of 213 inhibitory neuron (IN)  
776 morphologies (203 labeled in L2-6 *in vitro* <sup>53, 54, 55</sup>, 10 labeled in L1 *in vivo* <sup>56</sup>) to the geometric model of  
777 wS1. Combining these data by using a previously reported network building approach <sup>25</sup>, we generated  
778 a structurally dense model of wS1, which comprised soma, dendrite and axon morphologies that  
779 represent all of the excitatory (here: 462,402) and inhibitory neurons (here: 67,535) that are located in rat  
780 wS1, as well as axon morphologies that represent the IC part of all VPM neurons (here: 6,225). To  
781 estimate synaptic connectivity within this structurally dense wS1 model, we calculated the overlap at 50  
782  $\mu\text{m}^3$  resolution between the putative postsynaptic target structures (PSTs; i.e., soma/dendrite surface for  
783 inhibitory connections; dendritic spines for excitatory connections) and putative presynaptic sites (i.e.,  
784 axonal boutons) for all pairs of neurons, and normalized this quantity by the respective total amount of  
785 locally available PSTs (i.e., total somatic/dendritic surface and number of spines within each 50  $\mu\text{m}$   
786 voxel). Neglecting wiring specificity at subcellular scales <sup>25</sup>, we converted these overlap measurements

787 into connection probabilities, which predict the respective distributions of the numbers and most likely  
788 dendritic locations of synaptic contacts. To compare the predicted connection probabilities between  
789 excitatory IC cell types and L5PTs with previously reported paired-recording results that were obtained  
790 from acute brain slices *in vitro*, we cropped out ten 300  $\mu\text{m}$  wide thalamocortical/semi-coronal slices from  
791 the network model, which comprised at least half of the C2 barrel column volume. Connection  
792 probabilities that were predicted for truncated morphologies in slices are denoted by asterisks in **Table**  
793 **S3**. To compare the predicted connection probabilities between TC neurons and L5PTs with previously  
794 reported paired-recording results that were obtained *in vivo*, we used L5PTs whose somata were closest  
795 to the C2 barrel column (i.e., including septal neurons) and TC neurons located in the C2 VPM-barreloid  
796 of the uncropped network model. To compare the predicted connection probabilities between INs and  
797 L5PTs with previously reported paired-recording results we grouped all excitatory neurons in layer 5 (i.e.,  
798 L5PTs and L5ITs) whose somata were closest to the C2 barrel column (i.e., including septal neurons)  
799 and INs whose axons remained largely confined to layer 5. Finally, we embedded the L5PT model into  
800 the network model of wS1 by using a previously reported registration approach<sup>9</sup>. Here, we placed the  
801 L5PT model at nine different locations within the barrel column representing the C2 whisker (i.e.,  
802 approximately in the center of wS1), while preserving its (*in vivo*) soma depth location. For each of the  
803 nine locations (i.e., one in the column center, and eight at equally spaced angular intervals with a distance  
804 of  $\sim 100 \mu\text{m}$  to the column center) we used the connectivity mapping procedures as described above to  
805 estimate the numbers and dendritic locations of cell type-specific synaptic inputs that impinge onto the  
806 dendrites of the L5PT model. Specifically, by sampling from the overlap distributions 50 times, calculating  
807 the mean of the number of synaptic inputs from each cell type, and choosing the sample that was closest  
808 to this mean, we estimated that the L5PT model receives a total of  $24,161 \pm 785$  synaptic inputs. Of  
809 those,  $\sim 90\%$  are predicted to originate from excitatory IC and TC neurons, which corresponds to an  
810 average density of 1.4 glutamatergic and 0.14 GABAergic synapses per  $\mu\text{m}$  dendrite, respectively (i.e.,  
811  $148 \pm 18$  GABAergic synapses are located on the soma).

812

813 **Synapse models:** Conductance-based synapses were modeled with a double-exponential time course.  
814 Excitatory synapses contained both AMPA receptors (AMPA) and NMDARs. Inhibitory synapses  
815 contained GABA<sub>A</sub>Rs. The reversal potential of AMPARs and NMDARs was set to 0 mV, that of GABA<sub>A</sub>Rs  
816 to -75 mV. Rise and decay time constants of AMPARs were set to 0.1 ms and 2 ms, respectively<sup>57</sup>; those  
817 of NMDARs to 2 ms and 26 ms, respectively<sup>57</sup>; and those of GABA<sub>A</sub>Rs to 1 ms and 20 ms, respectively  
818<sup>58</sup>. The Mg-block of NMDARs was modeled by multiplying the conductance value with an additional  
819 voltage-dependent factor  $1/(1 + \eta \cdot \exp(-\gamma \cdot V))$ <sup>59</sup>, where  $\eta = 0.25$ ,  $\gamma = 0.08/\text{mV}$ , and  $V$  is the membrane  
820 potential in mV<sup>60</sup>. The peak conductance at excitatory synapses from different presynaptic cell types was

821 determined by assigning the same peak conductance to all synapses of the same cell type, activating all  
822 connections of the same cell type (i.e., all synapses originating from the same presynaptic neurons) one  
823 at a time, and comparing parameters of the resulting unitary postsynaptic potential (uPSP) amplitude  
824 distribution (mean, median and maximum) for a fixed peak conductance with experimental  
825 measurements *in vitro* (input from L2-6<sup>61</sup>) or *in vivo* (TC input<sup>7</sup>). The peak conductance for synaptic  
826 inputs from each cell type was systematically varied until the squared differences between the parameters  
827 of the *in silico* and *in vitro/in vivo* uPSP amplitude distributions were minimized (**Table S4**). The peak  
828 conductance at inhibitory synapses was fixed at 1 nS<sup>35</sup>. Release probability at excitatory and inhibitory  
829 synapses was fixed at 0.6 and 0.25, respectively<sup>35, 62</sup>.

830

831 **Synaptic input patterns:** Synaptic input patterns to the L5PT model were estimated as follows: All  
832 presynaptic neurons determined during the network-embedding procedure were converted into point  
833 neurons that could emit APs. During periods of ongoing activity, APs in presynaptic neurons were  
834 modeled as Poisson trains with cell type-specific mean firing rates as measured *in vivo*<sup>13</sup>. The mean  
835 firing rate of INs was set to 7 Hz<sup>35</sup> (except for L1 INs<sup>56</sup>). Each AP in a presynaptic neuron is registered  
836 at all synapses between the presynaptic neuron and the L5PT model without delay and may cause a  
837 conductance change, depending on the release probability of the synapse. After a stimulus (i.e.,  
838 deflection of the PW, SW or MW), each presynaptic neuron can emit additional spikes. The location of  
839 the deflected whisker in the wRF of the presynaptic neuron is determined based on the barrel column  
840 where the soma of the presynaptic neuron is located in (i.e., a convolution operation), and the  
841 corresponding whisker-specific post-stimulus time histogram (PSTH) is used to stochastically generate  
842 additional sensory-evoked APs. Whisker-specific PSTHs of excitatory cell types were generated based  
843 on *in vivo* wRF measurements (**Fig. S3**). The amplitude of the PSTH of excitatory IC cell types is further  
844 scaled by a factor of 0.4571 to reflect lower response probabilities of cortical neurons in the up-state<sup>63</sup>.  
845 The whisker-specific PSTHs of TC neurons in VPM were constructed based on previously published *in*  
846 *vivo* measurements, where single- and multi-whisker responsive neurons were described for the same  
847 experimental conditions used in this study<sup>23</sup>. Single- and multi-whisker responsive VPM neurons were  
848 grouped into a single TC PSTH. The whisker-specific PSTHs of INs in wS1 were constructed based on  
849 previously published *in vivo* measurements, which were acquired under the same experimental  
850 conditions that were used here<sup>26, 64</sup>, and which can be summarized as follows: (1) the onset times of  
851 whisker-evoked APs in INs across all layers should be similar to those of the excitatory cell types; (2) in  
852 case of PW touch, AP onset times in INs should precede those of the excitatory IC, but not TC cell types;  
853 (3) INs have broad wRFs. To capture these empirical constraints, the PW/SW-evoked PSTHs of INs were  
854 set to the respective maximum values across all excitatory cell types in each 1 ms time bin; the resultant

855 PW-evoked PSTH was shifted by -1 ms (but no spiking before TC neurons; i.e., > 8 ms); and the ratio  
856 between the integrals of the PW- and SW-evoked PSTHs during 0-50 ms was set to a fixed ratio of 2:1.  
857 These constraints leave one free parameter for constructing the PSTHs of INs: the total number of PW-  
858 evoked APs during 0-50 ms post stimulus. We simulated the response of the L5PT model after PW  
859 deflections while systematically varying this parameter, and computed the resulting number of APs during  
860 0-25 ms, until the L5PT model exhibited simulation trials with and without AP responses as measured *in*  
861 *vivo*. This yielded a value for INs of 1.0 APs per PW deflection per 50 ms. *In silico* pharmacology  
862 experiments were performed by removing all synaptic inputs from specific presynaptic populations from  
863 the model as shown in **Fig. 5D**.

864

865 **Simulations:** We generated 200 samples of structurally- and functionally-plausible cellular stimulus  
866 representations for each of the nine L5PT model locations (i.e., 1,800 samples per whisker), and for each  
867 simulated whisker deflection in the control condition (i.e., the complete network model), and for three  
868 different *in silico* pharmacology experiments. Since the L5PT model was located in the C2 column,  
869 simulated C2 deflections were assigned as PW deflections, those of the eight adjacent whiskers as SW  
870 deflections, and simulated E2 deflections as MW deflections. The three different *in silico* pharmacology  
871 conditions were as follows: (1) synapses from border stratum (L5/6BS) cells whose somata were located  
872 within the E2 column or the surrounding septum were removed from the L5PT model; (2) synapses from  
873 neurons of all excitatory cell types whose somata were located within the E2 column, except for L5/6BS  
874 cells, were removed; (3) synapses from all L5/6BS cells throughout wS1 were removed. All combinations  
875 of L5PT model location, identity of the deflected whisker, and pharmacology condition resulted in 72,000  
876 spatiotemporal synaptic input patterns, which we associate with different trials. For each trial, we  
877 numerically simulated the integration of the respective conductance changes within all dendritic  
878 compartments (and the soma and axon) of the HH-type L5PT model. Each simulation trial consisted of  
879 245 ms ongoing activity, followed by 50 ms of sensory-evoked activity. The first 100 ms and the last 25  
880 ms of simulated activity were discarded. AP times were determined from zero-crossings of the simulated  
881 membrane potential at the soma. For each of the simulation trials (control condition) we created a 100-  
882 dimensional vector, which quantified the spatiotemporal features of the respective synaptic input patterns  
883 that impinge onto the L5PT model. Entries of the vector represented all active synapses during the period  
884 of 0-25 ms post stimulus, their respective path length distances to the soma, times of activation with 1  
885 ms resolution, and whether the synapses originated from excitatory or inhibitory neurons. The input  
886 vectors were sorted into two groups, representing simulations in which onset APs (i.e., during the period  
887 of 8-25 ms post stimulus) did or did not occur. A principal component analysis (PCA) of these  
888 spatiotemporal input vectors revealed that trials with vs. without onset APs formed overlapping, but

889 systematically different distributions. PC<sub>1</sub> discriminated between these distributions. 92% of PC<sub>1</sub> could be  
890 accounted for by the difference between excitatory and inhibitory inputs that are active during a period of  
891 8-16 ms post stimulus, and that are located within less than 500  $\mu\text{m}$  path length distance to the soma  
892 (here referred to as proximal inputs). We defined a single quantity that represents PC<sub>1</sub> – synchronous  
893 proximal drive (SPD) – i.e., it reflects the net input (i.e., number of active excitatory minus active inhibitory  
894 synapses) along the proximal dendritic compartments of the L5PT model (i.e., path length distance <500  
895  $\mu\text{m}$ ) within 8-16 ms. We then calculated the probability of observing a whisker-evoked AP response in  
896 the L5PT model as a function of SPD, and fitted a sigmoidal curve to this distribution. The inverse width  
897 (or slope) of the fitted sigmoidal curve can be interpreted as a measure for the predictive power of SPD  
898 for AP responses. We systematically varied the end time point of the integration time window to determine  
899 the SPD window with highest predictive power, which matched closely with the SPD window determined  
900 for PW deflections by the PCA. These SPD windows were then used to compute the AUROC values for  
901 PW and SW deflections reported in the main text. Breaking down SPD into its two parameter, (1) the  
902 number of active excitatory synapses along the proximal dendrites, and (2) their respective synchrony  
903 (i.e., time window in which they are active), we performed additional simulations of the L5PT model. To  
904 do so, the structurally and functionally constrained PW/SW-evoked spatiotemporal synaptic input  
905 patterns were replaced as follows. All other model parameters (i.e., biophysical and synapse models), as  
906 well as synaptic input patterns preceding the stimulus remained unchanged. First, the distribution of  
907 stimulus evoked synaptic inputs along the dendrites of L5PT model was determined by calculating the  
908 average distribution of active synapses during 50 ms following PW and SW simulation trials (i.e., from  
909 the structurally and functional constrained trails). Second, the resultant 3D distributions of active  
910 excitatory and inhibitory synapses were converted into distance-dependent probability distributions (i.e.,  
911 1D) with 50  $\mu\text{m}$  (i.e., path length) resolution. Third, the subcellular distributions, temporal activation  
912 patterns and numbers of active synapses (i.e., excitatory/inhibitory during periods of ongoing activity;  
913 inhibitory during periods of whisker-evoked activity) were then determined by calculating the respective  
914 averages across PW and SW simulation trials (i.e., from the structurally and functional constrained trails),  
915 respectively. Fourth, the temporal distribution of active excitatory synapses was modeled as a log-normal  
916 distribution<sup>10</sup> with a fixed offset of 8 ms post-stimulus (i.e., corresponding to the onset latency of VPM  
917 input) and a fixed peak time of 9 ms post-stimulus. Fifth, the only remaining parameter was the median  
918 timing of the log-normal distribution. Varying this parameter in 1 ms steps resulted in excitatory synaptic  
919 input distributions that ranged from highly synchronous (2 ms; i.e., median timing at 10 ms post stimulus)  
920 toward asynchronous (i.e., median timing much later than 10 ms post stimulus). Sixth, at the same time,  
921 the total number of active excitatory synaptic inputs was systematically varied. Seventh, for each  
922 combination of the number and synchrony of stimulus evoked excitatory inputs, 200 samples of

923 spatiotemporal synaptic input patterns were generated and simulated as described above. Then, the  
924 probability of an onset AP (i.e., between 8-16 ms) was calculated for each combination of the number  
925 and synchrony of stimulus evoked excitatory inputs. Iso-AP probability contour plots were calculated by  
926 arranging all synaptic input number and synchrony combinations in a 2D grid, and linear interpolation  
927 between the grid points. The corresponding *in vivo* data of cell type-specific numbers and synchronies of  
928 active proximal inputs were derived from the structural and functional simulation constraints of PW, SW  
929 and MW deflections (i.e., representing our *in vivo* measurements (**Fig. S3**) and reconstructions of the  
930 network model (**Fig. S5**)).

931

932 **Statistical analysis:** All data are reported as mean  $\pm$  standard deviation unless mentioned otherwise.  
933 Normality was not assumed when performing statistical testing. All tests were performed using the R  
934 software package (version 3.4.3) and the scipy python package (version 1.0.1).

935

936 **Data availability:** All relevant data are available from the authors. The model and simulation routines,  
937 including a detailed documentation of all parameters and the analysis routines can be obtained from  
938 ModelDB (<http://senselab.med.yale.edu/ModelDB/>; accession number: 239145; password: Horizontal).

939 **Supplementary Materials for:**

940 Thalamus drives two complementary input strata of the neocortex in parallel

941

942 R. Egger<sup>1†‡</sup>, R.T. Narayanan<sup>1†</sup>, D. Udvary<sup>1</sup>, A. Bast<sup>1</sup>, J.M. Guest<sup>1</sup>, S. Das<sup>2</sup>, C.P.J. de Kock<sup>2</sup>, M.  
943 Oberlaender<sup>1\*</sup>

944

945 <sup>1</sup>Max Planck Group: In Silico Brain Sciences, Center of Advanced European Studies and Research,  
946 Bonn, Germany; <sup>2</sup>Department of Integrative Neurophysiology, Center for Neurogenomics and Cognitive  
947 Research, VU Amsterdam, The Netherlands.

948

949 \*Correspondence to: [marcel.oberlaender@caesar.de](mailto:marcel.oberlaender@caesar.de);

950 †These authors contributed equally.

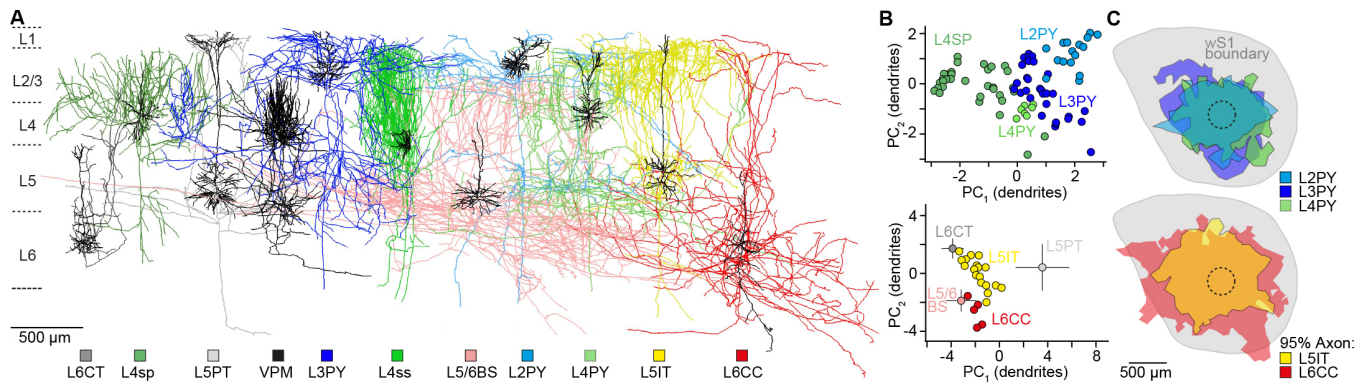
951 ‡Current address: Neuroscience Institute, NYU School of Medicine, New York, USA.

952

953 **The Supplement includes:** Figures S1 to S6

954 Tables S1 to S4

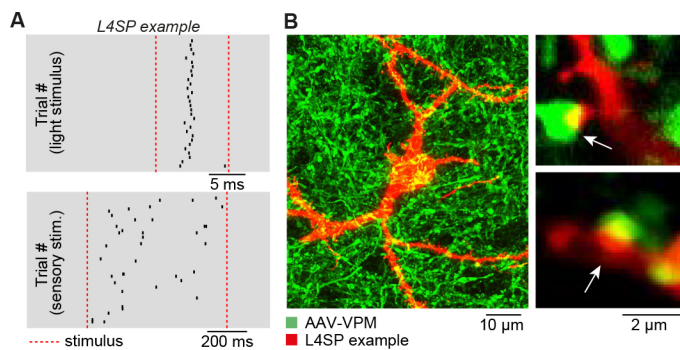
955 Movie S1



956

957 **Figure S1: Cell type-specific structural constraints for *in silico* experiments.** **A)** Gallery of exemplary  
 958 *in vivo* labeled neuron morphologies for each of the 10 major excitatory cell types of the neocortex, whose  
 959 soma, dendrite and axon distributions (ICs, n=177) were compared with the laminar distribution of  
 960 thalamocortical axons from the ventral posterior medial nucleus (VPM, n=14). Neurons were classified  
 961 as reported previously<sup>12</sup> into pyramidal neurons in layer 2 (L2PY, n=16), layer 3 (L3PY, n=30) and layer  
 962 4 (L4PY, n=7), spiny stellates (L4ss, n=22) and star-pyramids in layer 4 (L4sp, n=15), slender-tufted  
 963 intratelencephalic (L5IT, n=18) and thick-tufted pyramidal tract neurons in layer 5 (L5PT, n=37),  
 964 corticothalamic (L6CT, n=13) and polymorphic corticocortical neurons in layer 6 (L6CC, n=5), and  
 965 corticocortical neurons at the layer 5/6 border (L5/6BS, n= 14). L4ss and L4sp neurons were grouped as  
 966 layer 4 spiny neurons (L4SP). **B)** Principal components (PC<sub>1/2</sub>) of dendritic features that discriminate  
 967 between excitatory cell types in the upper and deep layers, respectively. The means and STDs of L5/6BS,  
 968 L5PT and L6CT neurons from **Fig. 1C** are shown for comparison. **D)** Horizontal axon extent of L2PY  
 969 (n=9), L3PY (n=15), L4PY (n=4), L5IT (n=5) and L6CC (n=4) neurons.

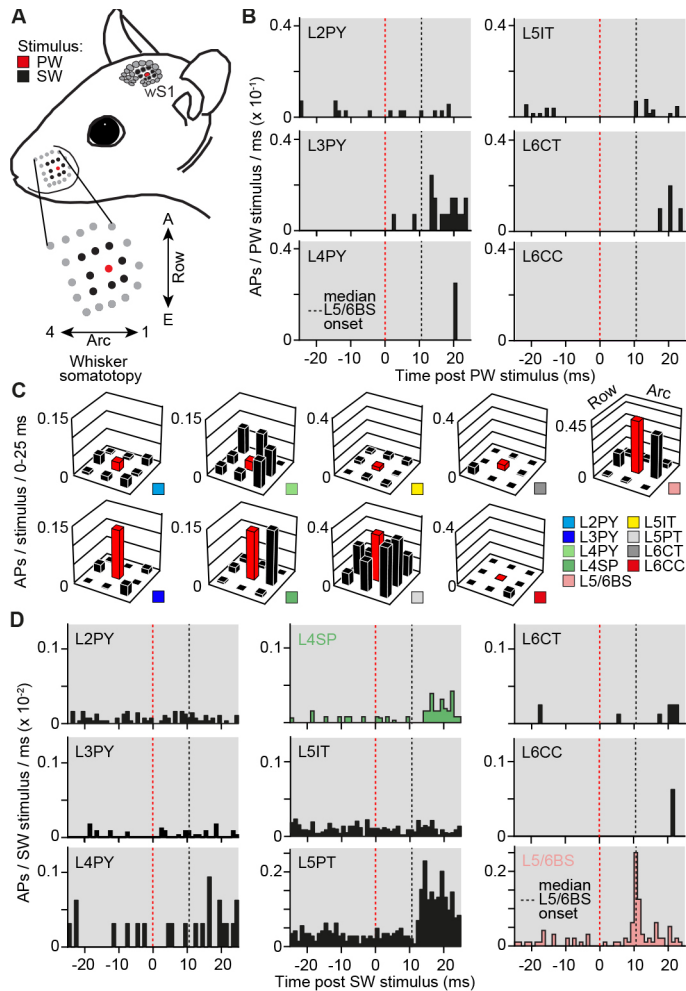
970



971

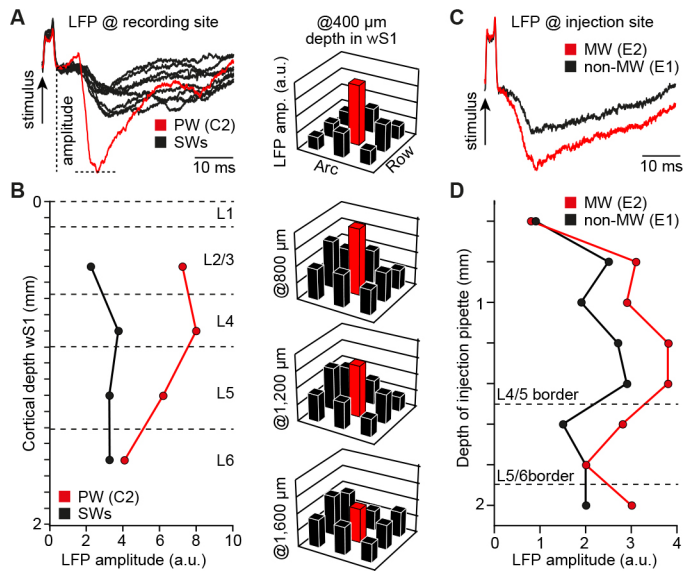
972 **Figure S2: Thalamocortical input to L4SP cells.** **A)** Example of cell-attached *in vivo* recording in layer  
 973 4 of wS1 of AAV-injected brain. Ticks represent APs in response to a 10 ms flash of green light onto the  
 974 cortical surface (top), and a 700 ms airpuff onto the whiskers (bottom). **B)** Confocal images of the neuron  
 975 shown in panel A. The neuron was morphologically identified as L4SP. Putative thalamocortical synapses  
 976 were identified as contacts between VPM boutons and dendritic spines.





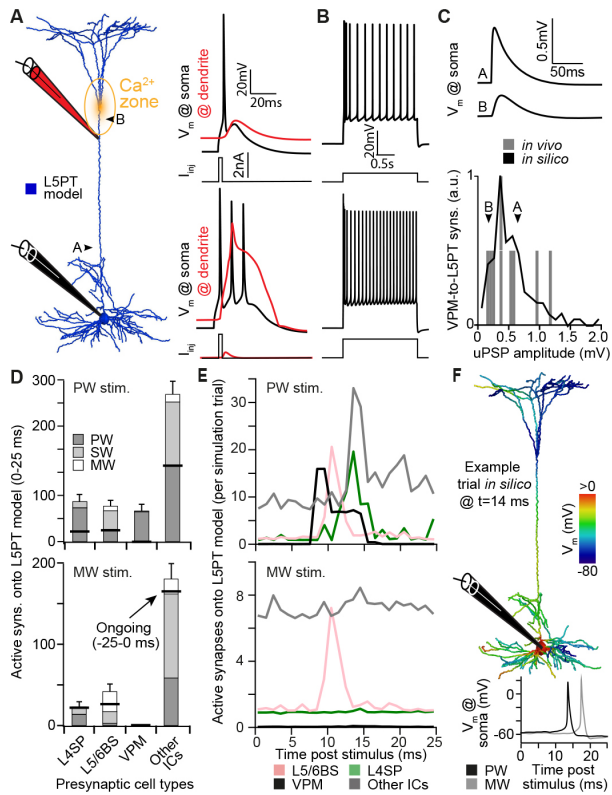
977

978 **Figure S3: Cell type-specific functional constraints for *in silico* experiments.** **A**) Illustration of cell  
 979 type-specific mapping of whisker receptive fields (wRFs) as reported previously<sup>10</sup> (i.e., under conditions  
 980 that were consistent with those of the pharmacological manipulations). Action potentials (APs) were  
 981 recorded in responses to deflections of the principal whisker (PW), and of the eight whiskers that are  
 982 adjacent to the PW (here referred to as SWs). **B**) PSTHs of PW-evoked APs for morphologically classified  
 983 L2PY (n=7), L3PY (n=7), L4PY (n=2), L5IT (n=13), L6CT (n=5) and L6CC (n=1) neurons, analogous to  
 984 those shown in **Fig. 3C** for L4SP, L5PT and L5/6BS neurons. **C**) Cell type-specific wRFs representing  
 985 the cells in panels B and D. **D**) PSTHs of SW-evoked APs for all cell types (i.e., averaged across the  
 986 adjacent whiskers), representing the cells shown in panels B and C, and **Fig. 3C**.



987

988 **Figure S4: LFP guided *in vivo* pharmacology.** **A)** Left panel: LFP recordings via search pipette at 400  
 989  $\mu\text{m}$  depth in wS1. LFP amplitudes in response to deflections of the PW and its eight SWs were quantified.  
 990 Right panel: LFP wRF reveals the PW at the recording site <sup>24</sup> (here: C2). **B.** LFP wRF measurements  
 991 were repeated at different cortical depths of wS1. Using the depth of layer borders <sup>11</sup>, the characteristic  
 992 laminar profiles of LFP responses to PW (and SW) stimuli were used to identify the border between layer  
 993 4 and 5 (i.e.,  $\sim 100 \mu\text{m}$  below the LFP maximum). The target location at the L5/6 border was hence  
 994 approximately 400-500  $\mu\text{m}$  below the LFP maximum. **C-D).** Example experiment that illustrates how the  
 995 LFP depth profile was used to locate the L5/6 border of the barrel column representing the MW whisker  
 996 (i.e., E2). The muscimol injection pipette was inserted rostral to wS1 at an angle that was approximately  
 997 parallel to the midline (i.e., oblique to the vertical axis of wS1). E2 was identified as the MW based on the  
 998 larger LFP amplitudes across the cortical depth when compared to those evoked by SW stimuli (shown  
 999 here: E1). The target location (i.e., L5/6 border) was then determined by identifying the depth of maximal  
 1000 LFP amplitude and adding 500  $\mu\text{m}$  (i.e., here injection at  $\sim 1850 \mu\text{m}$  depth).



1001

1002

1003

1004

1005

1006

1007

1008

1009

1010

1011

1012

1013

1014

1015

1016

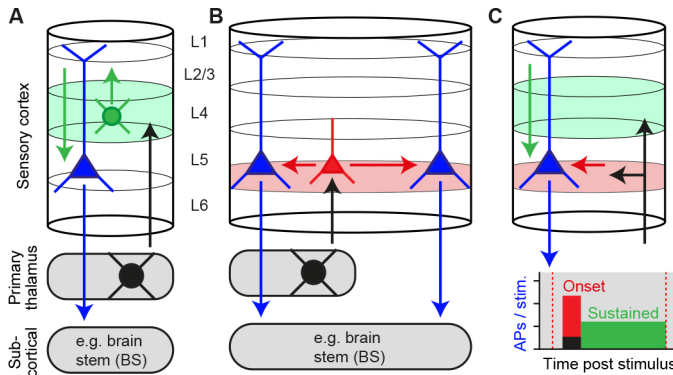
1017

1018

1019

**Figure S5: Intrinsic physiological and synaptic constrains for *in silico* experiments. **A**) Left panel: L5PT neuron model, consisting of 1033 dendritic compartments with previously reported biophysical models<sup>27</sup>. The parameters of the biophysical models were tuned until numerical simulations reproduced current injection-evoked responses that are characteristic for L5PT neurons (right panels): (1) a brief current injection into the soma triggers an AP that back-propagates into the apical dendrite (bAP), and (2) a brief current injection into the soma, followed by current injection into a  $Ca^{2+}$  channel dense region around the first bifurcation point of the apical tuft, triggers somatic bursts (i.e., BAC firing). **B**) The model supported regular AP firing of increasing frequencies in response to sustained current injections of increasing amplitude. **C**) The peak conductance at excitatory synapses from different presynaptic cell types was optimized to match empirical unitary post-synaptic-potential (uPSP) amplitude distributions (here exemplified for VPM-to-L5PT synapses<sup>7</sup>). **D**) The neuron model was embedded into an anatomically realistic network model of rat wS1 and VPM. Based on cell type-specific axo-dendritic overlap (using the morphologies shown in **Fig. 1** and **Fig. S1**) and wRF measurements (**Fig 3** and **Fig. S3**), plausible synaptic input patterns to the L5PT neuron model were generate for deflections of different whiskers. The number (mean  $\pm$  STD across simulation trials) of active synapses that impinge onto the neuron model during the first 25 ms after simulations of PW and MW deflections are shown. Horizontal black lines denote the number of active synapses that each cell type contributes also to 25 ms of ongoing activity (i.e., before the stimulus). Different grey shadings denote the location of the presynaptic neurons**

1020 (i.e., somatotopically aligned with the PW, SW or MW). **E**) The number (mean across simulation trials) of  
1021 active synapses that impinge onto the neuron model during each millisecond of the first 25 ms after  
1022 simulations of PW and MW deflections, respectively. Other ICs represent inputs from all excitatory  
1023 intracortical cell types, except for the border stratum cells. **F**) Exemplary simulation trial for synaptic input  
1024 patterns as shown in panels D and E, which are integrated by the dendrites of the L5PT neuron model  
1025 (upper panel) and transformed into somatic APs (lower panel).  
1026



1027 **Figure S6: Suggested concept of primary sensory cortex.** Sensory-evoked thalamocortical input is  
1028 relayed in parallel by two orthogonally organized thalamorecipient populations which give rise to  
1029 complementary canonical pathways: vertical to layers 2/3 by L4SP neurons (**A**), and horizontally to layers  
1030 5/6 by L5/6BS cells (**B**). The deep thalamorecipient pathway activates pyramidal tract neurons, whereas  
1031 signal flow in the upper layers terminates in layer 5. The complementary pathway theory hence provides  
1032 a potential explanation for sustained AP responses in pyramidal tract neurons that persist for the duration  
1033 of the stimulus. We showed that one way to drive cortical output is by providing sufficiently strong and  
1034 synchronous synaptic input to the proximal dendrites. However, synchrony decreases during recurrent  
1035 excitation within local and long-range cortical circuits. Moreover, a substantial fraction of these recurrent  
1036 and top-down inputs will impinge onto distal dendrites (e.g. within L1). It is hence unlikely that sustained  
1037 responses in pyramidal tract neurons originate from the same mechanism as the onset responses (see  
1038 also <sup>14</sup>). We thus hypothesize that the L5/6BS cell-driven onset responses are required to switch the  
1039 apical dendrites into an active state, which allows pyramidal tract neurons to transform temporally less  
1040 synchronous and spatially more distributed synaptic inputs (e.g. from layers 2/3) into sustained patterns.  
1041

1042

Parameter	Soma	AIS / Myelin	Apical dendrite	Basal dendrites
$C_m$ ( $\mu\text{F}/\text{cm}^2$ )	1.0	1.0 / 0.04	2.0	2.0
$r_a$ ( $\Omega\text{cm}$ )	100	100 / 100	100	100
$g_{\text{pas}}$ ( $1/r_m$ )	0.326	0.256 / 0.4	0.882	0.631
$\text{Na}_t$	24300	880 / –	252	–
$\text{Na}_p$	49.9	14.6 / –	–	–
$\text{K}_t$	471	841 / –	–	–
$\text{K}_p$	0	7730 / –	–	–
SKv3.1	9830	9580 / –	112	–
SK E2	492	0.577 / –	34	–
$\text{Ca}_{\text{LVA}}$	46.2	85.8 / –	1040*	–
$\text{Ca}_{\text{HVA}}$	6.42	6.92 / –	45.2*	–
$\tau_{\text{Ca}}$ (ms)	770	507 / –	133	–
$\gamma_{\text{Ca}}$ (1)	0.000616	0.0175 / –	0.0005	–
$I_m$	–	– / –	1.79	–
$I_h$	0.8	0.8 / –	$A+B \cdot \exp(C \cdot d/d_{\text{max}})$ **	2

1064

1065 **Table S1.** Biophysical parameters of the L5PT model. These parameters were obtained using the multi-  
 1066 objective optimization algorithm described previously<sup>27, 51</sup>. Units for different ion channel densities are  
 1067  $\text{pS}/\mu\text{m}^2$ .  $\tau_{\text{Ca}}$  (ms) is the time constant of the calcium buffering model, and  $\gamma_{\text{Ca}}$  is a dimensionless parameter  
 1068 describing the calcium buffer affinity.  $g_{\text{pas}}$ : passive membrane conductance;  $\text{Na}_t$ : fast inactivating sodium  
 1069 current;  $\text{Na}_p$ : persistent sodium current;  $\text{K}_t$ : fast inactivating potassium current;  $\text{K}_p$ : slow inactivating  
 1070 potassium current; SKv3.1: fast non-inactivating potassium current; SK E2: calcium-activated potassium  
 1071 current;  $\text{Ca}_{\text{LVA}}$ : low voltage-activated calcium current;  $\text{Ca}_{\text{HVA}}$ : high voltage-activated calcium current;  $I_m$ :  
 1072 muscarinic potassium current;  $I_h$ : non-specific cation current. \* Density in the calcium “hot zone” between  
 1073 900-1100  $\mu\text{m}$  from the soma. The density of low- and high-voltage activated calcium channels in the  
 1074 apical dendrite was set to 1% and 10% of that value, respectively, outside of the “hot zone”. \*\* The density  
 1075 of  $I_h$  in the apical dendrite increases exponentially with distance  $d$  to the soma, with parameters  $A = -$

1076 0.8696 pS/ $\mu\text{m}^2$ , B = 2.087pS/ $\mu\text{m}^2$ , C=3.6161, and  $d_{\text{max}}$  the distance of the apical dendrite top located the  
1077 furthest from the soma. Voltage- and time-dependence of ion channels was modeled using the HH  
1078 formalism. All corresponding parameters were taken from the literature and have been described in detail  
1079 previously<sup>27</sup>.

Feature	Mean $\pm$ STD	Model	Difference (STD)
Ca <sup>2+</sup> AP peak	6.73 $\pm$ 2.54mV	10.8mV	1.6
Ca <sup>2+</sup> AP width	37.43 $\pm$ 1.27ms	36.5ms	0.7
BAC AP count	3 $\pm$ 0	3	0
Mean somatic AP ISI	9.9 $\pm$ 0.85ms	9.4ms	0.6
Somatic AHP depth	-65 $\pm$ 4mV	-66mV	0.3
Somatic AP peak	25 $\pm$ 5mV	34mV	1.8
Somatic AP half-width	2 $\pm$ 0.5ms	1.6ms	0.8
AP count (somatic current injection only)	1 $\pm$ 0	1	0
bAP amplitude at 835 $\mu$ m from the soma	45 $\pm$ 10mV	14mV	3.1
bAP amplitude at 1015 $\mu$ m from the soma	36 $\pm$ 9.33mV	9mV	2.9

1098 **Table S2.** Features of membrane potential used to constrain the intrinsic physiology of the L5PT model.  
 1099 Empirical features were adapted as reported previously <sup>27</sup>. ISI: inter-spike interval; AHP: after-  
 1100 hyperpolarization. Model features based on optimized parameters (see **Table S1**). Difference between  
 1101 model features and average experimental features given in units of STD of the experimental features.  
 1102 The recording locations for the bAP amplitude were adjusted to account for a longer apical trunk of the  
 1103 present L5PT morphology.

Presynaptic cell type	Measurement (Reference)	Network model (L5PT population)	Network model (L5PT model)
L2PY	0.08 <sup>65</sup>	0.06 ± 0.09*	0.13 ± 0.02
L3PY	0.12/0.55 <sup>65, 66</sup>	0.14 ± 0.16*	0.34 ± 0.02
L4 (SP, PY)	0.08 <sup>65</sup>	0.14 ± 0.16*	0.33 ± 0.04
L5IT	0.19 <sup>67</sup>	0.18 ± 0.13*	0.19 ± 0.05
L5PT	0.05-0.2 <sup>67, 68, 69</sup>	0.23 ± 0.18*	0.24 ± 0.06
L6 (BS, CT)	0.02 <sup>65</sup>	0.14 ± 0.15*	0.15 ± 0.02
VPM	0.44 ± 0.17 <sup>7</sup>	0.40 ± 0.12	0.39 ± 0.05
IN	0.22 <sup>70</sup>	0.41 ± 0.14	0.26 ± 0.02

1117 **Table S3.** Comparison between predicted connection probabilities in wS1 network model and previously  
1118 reported measurements from paired-recordings *in vitro* or *in vivo*. The \* denotes predicted connection  
1119 probabilities between truncated morphologies in 300 µm wide thalamocortical/semi-coronal slices of  
1120 network model.



Cell type	uPSP Mean (mV) (exp. / fit)	uPSP Median (mV) (exp. / fit)	uPSP Max. (mV) (exp. / fit)	Conductance per synapse (nS)
L2PY	0.49 / 0.43	0.35 / 0.37	1.90 / 2.50	1.47
L3PY	0.49 / 0.44	0.35 / 0.39	1.90 / 1.98	1.68
L4 (SP, PY)	0.35 / 0.35	0.33 / 0.30	1.00 / 1.41	1.14
L5IT	0.47 / 0.40	0.33 / 0.35	1.25 / 1.70	1.38
L5PT	0.46 / 0.43	0.36 / 0.39	1.50 / 1.46	1.59
L6 (BS, CC)	0.44 / 0.42	0.31 / 0.40	1.80 / 1.26	1.63
L6CT	0.44 / 0.39	0.31 / 0.36	1.80 / 1.73	1.80
VPM	0.571 / 0.51	0.463 / 0.44	1.18 / 1.80	1.78

1121 **Table S4.** Features of uPSP distributions of L5PTs for synaptic input from each presynaptic excitatory  
1122 cell type, and the respectively fitted synaptic conductance values. Empirical values for uPSP amplitude  
1123 distributions of synapses from IC cell types <sup>61</sup> and VPM thalamus <sup>7</sup> were adapted as reported previously.

1124

1125 <https://www.dropbox.com/s/tg2kl837homq4dp/V11.mp4?dl=0>

1126 **Movie S1:** Examples of *in silico* pharmacology experiments.